Fundamental Test of a Hovering Rotor: Comprehensive Measurements for CFD Validation

Thomas R. Norman
Aerospace Engineer
NASA Ames Research Center
Moffett Field, CA USA

James T. Heineck
Physical Scientist
NASA Ames Research Center
Moffett Field, CA USA

Edward T. Schairer
Aerospace Engineer
NASA Ames Research Center
Moffett Field, CA USA

Norman W. Schaeffler
Research AST, Fluid Mechanics
NASA Langley Research Center
Hampton, VA USA

Lauren N. Wagner
Aerospace Engineer
NASA Ames Research Center
Moffett Field, CA USA

Gloria K. Yamauchi
Aerospace Engineer
NASA Ames Research Center
Moffett Field, CA USA

Austin D. Overmeyer
Research Scientist
U.S. Army Combat Capabilities Development Command
Aviation & Missile Center
Hampton, VA USA

Manikandan Ramasamy
Research Scientist
U.S. Army Combat Capabilities Development Command
Aviation & Missile Center
Moffett Field, CA USA

Christopher G. Cameron
Research Scientist
U.S. Army Combat Capabilities Development Command
Aviation & Missile Center
Moffett Field, CA USA

Michelle Dominguez
Aerospace Engineer
NASA Ames Research Center
Moffett Field, CA USA

Alex L. Sheikman
Instrumentation Engineer
NASA Ames Research Center
Moffett Field, CA USA

ABSTRACT

A model-scale hover test of a 4-bladed, 11.08-ft diameter rotor was recently completed inside the National Full-Scale Aerodynamics Complex 80- by 120-Foot Wind Tunnel test section. The primary objective of the test was to acquire key experimental data for a hovering rotor of sufficient quality and quantity to allow validation of state-of-the-art analysis codes. A comprehensive measurement set has been acquired, including rotor performance, blade airloads, flow transition locations, blade deflections, and wake geometry for a range of tip Mach numbers and collective settings. The present paper provides an overview of the test, including detailed descriptions of the hardware, instrumentation, and measurement systems. In addition, the specific test objectives, approach, and sample results are presented. The full test database, as well as detailed rotor geometry information, will ultimately be shared openly on a NASA-sponsored website to serve as a benchmark validation dataset.

NOTATION

a_∞	free-stream speed of sound, ft/s
A	rotor disk area, πR^2, ft^2
c	section blade chord, ft
C_p	blade pressure coefficient, $(p-p_\infty)/(1/2\rho\ (\Omega r)^2)$
C_Q	rotor torque coefficient, $Q/\rho\ (\Omega R)^2\ AR$
C_T	rotor thrust coefficient, $T/\rho\ (\Omega R)^2\ A$
DZ	out-of-plane bending, in
FM	figure of merit, $(C_T/2)^{1/2}\ C_T/C_Q$
g(i,j)	pixel grayscale value
G(i,j)	grayscale gradient value
i,j	column/row coordinate of image
M_{tip}	hover tip Mach number, $\Omega R/a_\infty$
p	blade surface pressure, lbf/ft^2
p_∞	free stream static pressure, lbf/ft^2
Q	rotor torque, ft-lbf
r	radial coordinate from hub center, ft
R	rotor radius, ft
T	rotor thrust, lbf
x	chordwise coordinate from leading edge, ft
z	axial coordinate from tip path plane, ft
ψ	rotor azimuth angle, deg
ρ	free-stream density, $slugs/ft^3$
Ω	rotor angular rotation rate, rad/s
σ	geometric rotor solidity
θ_0	collective pitch angle, deg

INTRODUCTION

Conventional rotary wing vehicles, including helicopters and tiltrotors, are designed for a wide variety of flight conditions with differing design objectives. These include efficient

Presented at the Vertical Flight Society's 79th Annual Forum & Technology Display, West Palm Beach, FL, USA, May 16-18, 2023.

cruise, hovering flight, and high-performance maneuvering. Accurate numerical predictions of performance in each of these areas are important for both the design of new vehicles as well as evaluation of legacy aircraft. The prediction of hovering performance is especially important, as it is typically the limiting design point in terms of power requirements. For the emerging market of Urban Air Mobility (UAM) vehicles, with multiple rotors and unconventional designs, accurate hover performance predictions are equally important, if not more so. For the U.S. Army Future Vertical Lift (FVL) family of vehicles, the hover condition is a critical design point regardless of the gross weight or rotor configuration. Hover power requirements remain the limiting design point, and inaccurate estimates can have significant negative effects on vehicle capabilities (especially when powered by heavy electrical systems/batteries).

The capability to predict hover performance consistently and reliably for a new rotor system has been elusive. Limitations in the numerical methods and/or the validation data sets have historically resulted in best-case prediction accuracies of 2-5% (Refs. 1-2). While this level of accuracy may be sufficient for some applications, it is ultimately not good enough for many DoD or UAM designs. For example, a 2% error in estimating the hover power required could severely limit the payload capability (one or two passengers depending on the size of the vehicle), or conversely, increase the weight and cost of building the aircraft. A prediction error of 0.5% is a much more useful goal.

Computational Fluid Dynamics (CFD) techniques offer the best opportunity to reach these hover prediction goals. Since 2014, the American Institute of Aeronautics and Astronautics (AIAA) has held a Rotorcraft Hover Prediction Workshop (HPW, Ref. 3) as part of the annual AIAA SciTech Forum to assess and advance the state-of-the-art CFD hover prediction methods. In 2017, Ref. 4 identified several prediction issues yet to be resolved, including those related to grid requirements (including grid independence), temporal accuracy requirements, solution convergence, wake breakdown, far-field boundary conditions, steady vs. unsteady solutions, and transition/turbulence modeling. In 2021, Ref. 5 noted that significant progress had been made in some areas, including in rotor wake preservation and transition modeling, but other questions remain. One of the biggest problems is that there is no publicly available data set that includes the key measurements needed for CFD validation (including performance, airloads, vortex trajectories, blade deformations, and transition locations).

High-quality data are ultimately necessary to adequately evaluate/validate the CFD predictions and to provide insight into the unresolved issues. Numerous hover data sets are available in the literature with more recent CFD comparisons focused on small-scale tests of the two-bladed Caradonna-Tung rotor (Ref. 6), the TRAM V-22 rotor (Refs. 7-8), and the UH-60 rotor (Refs. 9-10). In addition, as part of the AIAA Rotorcraft HPW, significant validation efforts have been made using data from small-scale S-76 tests (Refs. 11-12) and the Pressure Sensitive Paint (PSP) rotor (Ref. 13). While these data sets have proved invaluable for CFD evaluations to date, they each have limitations that make additional progress difficult. These limitations include the lack of a consistent set of critical measurements (airloads, transition locations, blade deformations, wake properties) and/or the lack of test hardware definition (rotor hub, rotor shaft and test support structure, ground and wall configuration, etc.).

To address these limitations and provide a new benchmark hover data set for CFD validation, NASA and the U.S. Army have recently completed testing of a 4-bladed, 11.08-ft diameter rotor in hover inside the 80- by 120-Foot Wind Tunnel test section of the U.S. Air Force National Full-Scale Aerodynamics Complex (NFAC). Details of this test are provided below, including test objectives, approach, test description, and sample results.

TEST OBJECTIVES AND APPROACH

The primary objective of the test was to acquire key experimental data for a hovering rotor of sufficient quality and quantity to allow validation of state-of-the-art analysis codes. During the initial planning for this test, the following key considerations helped guide the decision-making process:

1) The rotor should be representative of a “modern” multi-bladed helicopter with documented properties.
2) Test measurements should be sufficiently accurate for CFD validation (e.g., Figure of Merit, FM=±0.005) and comprehensive enough to ensure correct physics are represented (rotor performance, blade airloads, blade deformations, rotor wake geometry, and boundary layer transition state, etc.).
3) Experimental uncertainties due to effects that are not easily measurable (e.g., facility walls) should be minimized as much as practical.
4) Existing NASA/Army hardware and facilities should be utilized as much as possible (for cost and accessibility reasons).

Following an evaluation of available test stands and hover facilities, it was decided to design, build, and test a new pressure-instrumented 11.08-ft diameter rotor in the NFAC 80- by 120-Foot Wind Tunnel test section. The chosen rotor size results in reasonable tip Reynolds numbers (nominally 2.16×10^6 at 1250 RPM) while the facility size helps to minimize the effects of the ground/walls (see Refs. 14-15 for predicted effects). It was also decided that the comprehensive measurement set would include rotor performance, blade airloads, flow transition locations, blade deformations, and wake geometry. The performance measurements (thrust and torque) would be provided by the built-in rotor balance on the test stand, blade airloads by the pressure transducers on the new blade set, blade deformations using photogrammetry, flow transition locations using thermography, and wake geometry using shadowgraphy. Details describing the

hardware, instrumentation, and measurement techniques are provided in the following section.

DESCRIPTION OF THE EXPERIMENT

The test was conducted in the NFAC 80- by 120-Foot Wind Tunnel test section using an 11.08-ft diameter rotor system mounted on the Army Rotor Test Stand (ARTS). Figure 1 shows the model installed in the wind tunnel with the rotor at the tunnel centerline. In the following sections, detailed information is provided describing the experiment, including the test hardware, instrumentation, and data acquisition systems, as well as the independent measurement systems used for blade deformations, boundary layer transition, and wake geometry.

Figure 1. HVAB rotor mounted on ARTS test stand in the NFAC 80- by 120-Foot Wind Tunnel.

Hardware

The wind tunnel, test stand, and rotating hardware are described in the following section.

NFAC 80- by 120-Foot Wind Tunnel

The 80- by 120-Foot Wind Tunnel is part of the NFAC located at NASA Ames Research Center. The NFAC is managed and operated by the U.S. Air Force's Arnold Engineering Development Center (AEDC) under a long-term lease agreement with NASA. The open-return tunnel has a rectangular cross section and is lined with sound-absorbing material to reduce acoustic reflections. The actual test section dimensions are 79-ft high and 119-ft wide and the maximum test section velocity is approximately 100 knots. For the current test, the test section was used as a hover chamber, with the vane set in front of the fan drive closed to minimize crossflow due to external winds.

Army Rotor Test Stand (ARTS)

The ARTS, shown in Fig. 2, is a modular rotor test stand that was designed by the U.S. Army in the mid-1990s to test rotors ranging from 9-20 ft in diameter. A large range in rotor diameter was accommodated with variable motor power (200-800 HP), gear ratios (4.3-6.3:1), shaft lengths, force/moment balance ranges, swashplates, and hubs. Additional details of the ARTS are found in Ref. 16. The configuration used for this test could generate up to 400 HP, and included a 4.3:1 gear ratio transmission, short-shaft, and the VSB-68 rotor balance. The two 200-HP motors are combined via a two-stage transmission to drive the output shaft at the nominal rotor RPM. The output shaft is connected to a custom flex-coupler which is instrumented with torque and residual thrust full-bridge strain gages. All the shaft torque is transferred through the flex-coupler to the rotating spindle inside the VSB-68 balance. The spindle is supported by an upper thrust bearing and a lower set of duplex bearings. The spindle loads are transferred through the bearings to a series of axial beams in the VSB-68 balance which are gaged to measure the remaining three forces and two moments. A small fraction of the thrust load is carried in the flex-coupler and is used to correct the thrust measured by the normal force beams of the balance. The non-rotating swashplate and actuators mount to the non-rotating portion of the upper thrust bearing on the balance and the hub attaches to the balance spindle. The mounting arrangement results in a single load path from the rotor system to the balance.

Figure 2. ARTS test stand.

The non-rotating swashplate control actuators are brushless DC gearmotors with a spur gearbox and a self-locking drive screw to produce linear motion. Three actuators are used to control the inclination of the fixed swashplate and a fixed linear slider is used to prevent rotation. The swashplate slides via a monoball on a standpipe that surrounds the rotor shaft. The actuators are controlled via a pilot station in the control room. For hover testing, the pilot trimmed to the target conditions by adjusting collective pitch and setting cyclic pitch to zero.

The ARTS was mounted into the NFAC in a post-mount configuration as shown in Fig. 1, using both new and existing interface hardware. This resulted in the rotor plane being located 6.4 in above the tunnel centerline (480.4 in above the acoustically treated floor) and centered between the two tunnel sidewalls.

Rotating Hardware

The rotating hardware used for this test consisted of a four-bladed articulated rotor system (including hub, rotating control system and blades) and a rotating instrumentation hat (Figs. 2 and 3). Details of this hardware are presented below.

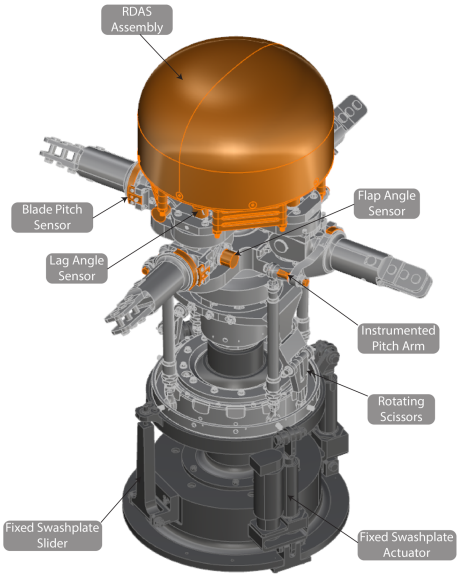

Figure 3. Schematic of rotating hardware including blade root angle sensors.

The hub is a fully articulated four-bladed hub with coincident flap/lag/pitch hinges (Fig. 3). The flap/lag hinges are located at 3.5 in rotor radius and blade feathering is supported by a tension-torsion strap. The hub is designed to support a 10,000 lbf blade centrifugal force which was required for the highly instrumented blades. A rotary damper is installed with a two-bar linkage between the lag hinge and damper axis which results in an approximately 2.6:1 amplification factor of the lag angle and a 6.76:1 amplification factor of the damping. The damper value was set to approximately 41.7 ft-lbf-s/rad resulting in a damping value of 282 ft-lbf-s/rad along the lag hinge. The pitch links are attached to a pitch arm stud aligned with the flap axis, resulting in zero flap-pitch coupling. The pitch studs were instrumented to measure the axial pitch link loads and the three root angles were measured for all four blades. The equivalent control system stiffness about the feathering axis (quarter-chord axis), which includes the fixed actuators, pitch links and pitch arm studs, was measured experimentally to be 1500-3000 ft-lbf/rad depending on the azimuthal position and the extent of the actuator.

The instrumentation hat, mounted on top of the hub, provided a location for terminating instrumentation wiring and mounting the Rotating Data Acquisition System (RDAS). Details of the RDAS are provided in the Instrumentation and Data Acquisition section below. The hat includes an aerodynamic fairing to protect these components as well as minimize undesirable aerodynamic forces.

A new pressure-instrumented rotor was developed for this test program. The Hover Validation and Acoustic Baseline (HVAB) blade set was designed as a four-bladed, articulated rotor with pressure and structural instrumentation. The rotor incorporates publicly available RC series airfoils and is geometrically identical (except for the blade root) to the Army PSP rotor previously tested at Langley Research Center (Refs. 13 and 17). A detailed description of the rotor, including the as-designed geometry, instrumentation, and structural properties, is provided in Ref. 18. General blade property and rotor planform information are provided in Table 1 and Fig. 4.

Table 1. HVAB Rotor Parameters

Parameter	Value
Number of blades	4
Radius, in	66.50
Blade chord, in	5.45
Rotor Geometric Solidity	0.1033
Rotor Airfoil	RC series
Blade Twist	Linear, -14 deg

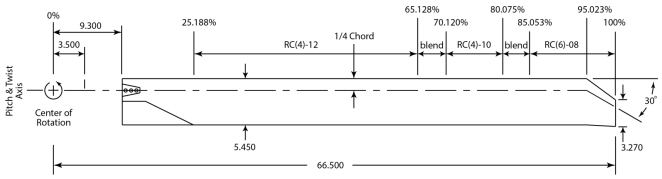

Figure 4. HVAB blade planform.

There are six blades in the HVAB blade set. Two of the blades feature unsteady pressure transducers, one blade is instrumented with four sets of strain gages along the span of the blade (SN005), and the last three blades are standard blades with only root strain gages for safety of flight (SN001, SN002, SN003). The first pressure-instrumented blade was designed to incorporate 187 unsteady pressure transducers, arranged in 11 chordwise stations consisting of 17 transducers each (SN004). The second pressure-instrumented blade was designed to incorporate a total of 51 unsteady pressure transducers arranged in two clusters near the leading edge at

two spanwise locations and was designed for future acoustics research (SN006). This second blade is not part of the current research effort. More details on the blade instrumentation for this rotor are provided in the next section.

One of the key rotor design requirements for the HVAB blade set was for blade uniformity despite the differences in instrumentation between blades. For each of the blades without pressure transducers, "dummy" transducers and wiring were installed in the same transducer locations that were defined for SN004. This resulted in a set of blades with essentially the same mass distribution along the blade radius. Each blade was also balanced against the reference blade, SN004, ensuring that the calculated centrifugal forces (assuming operation at the maximum operating RPM of 1310) were within ±5 lbf of the mean value for all the blades. Additionally, for the blades tested in this research effort, the measured natural frequencies for the first six modes were within ±5% of the average values across the set of blades.

Instrumentation and Data Acquisition Systems

This section describes the key measurements and data acquisition systems used to provide the rotor performance and blade airloads data acquired during this test. Descriptions of other key measurements, including the blade root motions, are also provided.

Rotor Performance Measurements and NFAC Data Acquisition System

As discussed earlier, the key rotor force and moment measurements were provided by the VSB-68 rotor balance and instrumented flex-coupler installed as part of the ARTS. The balance was recalibrated in 2019 at the NASA Langley balance calibration lab. First, the isolated flex-coupler residual thrust gage was calibrated in a single-axis calibration fixture. Next, the flex-coupler was installed in the VSB-68 balance with a rotational and normal force (thrust) lockout plate mounted to the end of the flex-coupler and the balance. A hub adapter and load arms, 42-in radius, were attached to the balance spindle. The lockout plate of the balance was mounted in a gantry load frame and oriented upright, inverted, and horizontal in all four roll angles. A series of combined loads were performed to generate a calibration matrix for the balance/flex-coupler resulting in the measured accuracies provided in Table 2. The balance calibration was particularly good for thrust and torque (the key measurements for this test), with dimensional accuracies of 1 lbf and 1 ft-lbf respectively. During testing, every effort was made to maintain these accuracies utilizing several processes, including in-situ checkloads, recording gage excitations, and applying shunt resistors.

In addition to the balance measurements, various atmospheric condition measurements (pressures and temperatures) were acquired to help derive the non-dimensional performance parameters. Rotor RPM (derived from a 1024/rev optical encoder installed at the bottom of the ARTS) was also a key measured parameter.

Table 2. VSB-68 Rotor Balance Accuracies

Force/Moment	Calibration Full-Scale (lbf) or (in-lbf)	Accuracy (%Full-Scale)
Normal (Thrust)	+3000/-500	0.03
Axial (Drag)	±1250	0.10
Pitch	±1250	1.32
Roll	±10,800	0.47
Yaw (Torque)	+13750/0	0.09
Side	±1250	0.31
Residual Thrust	±200	0.42

The NFAC Data Acquisition System (NFAC DAS) was the primary data acquisition system for much of the data acquired during this test, including the rotor balance measurements. Key features of this system include a large available channel count, variable sample rates based on the rotor RPM, and variable data record lengths, up to 256 revolutions. For this test, data were sampled at a rate of 256 samples/rev over a duration of 128 revolutions for each data point. The trigger signal for data acquisition was generated by the optical encoder mounted on the model, with the zero-degree reference position defined when the reference blade pointed along the rotor balance axial force direction (nominally downstream). In addition to this data acquisition function, the NFAC DAS provided real-time and post-point data reduction and processing capabilities (including safety monitoring).

Blade Pressures and Rotating Data Acquisition System

As discussed earlier, one of the HVAB blades was designed with 187 unsteady pressure transducers arranged in 11 chordwise stations of 17 transducers each (Ref. 18). A blade schematic showing the 11 radial stations is provided in Fig. 5. For each station, six of the transducers were located on the lower surface and 11 were located on the upper surface, with the first upper surface transducer being located at the leading edge of the blade. The blade stations were numbered in sequence starting at Station 1, which is closest to the root of the blade at 0.397R, and proceeding to Station 11, which is closest to the tip at 0.988R.

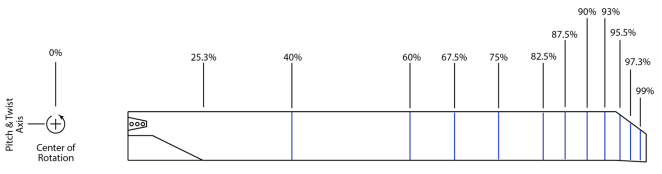

Figure 5. Locations of the pressure measurement stations on the HVAB pressure blade.

During testing, the voltages from the pressure transducers were acquired exclusively in the rotating frame by the hub-mounted Rotating Data Acquisition System (RDAS). The RDAS is a custom system designed and fabricated in 2009. It enables the simultaneous acquisition of 256 channels of data in the rotating frame and subsequent transfer of that data to a console unit, in the non-rotating frame, for logging. The transfer of data takes place through a fiber-optic rotary joint, which is integrated into the slip ring assembly.

The hub-mounted portion of the RDAS is referred to as the Remote and consists of a stack of five PCB boards. The motherboard is at the bottom with four 64-channel data acquisition boards stacked above (for a total of 256 channels). Each of the channels has its own programmable amplification and conditioning circuitry and analog-to-digital convertor. All 256 channels are simultaneously sampled at a rate of 48,800 samples per second. The Remote continuously samples data while powered on and transmits data down to the Console through the fiber-optic joint. Each dataset transferred represents the data for all 256 channels for that clock pulse.

The Console unit receives the sampled data from the fiber-optic joint and, if in a triggered state, packages the logged data into Ethernet packets and transfers them to a host PC via a direct Ethernet connection. During testing, the Console was triggered to log data over the same period as the NFAC data system so that the same 128 revolutions of data were acquired by both systems. To align the data, there were four timing signals that were acquired by both systems. Three of these timing signals varied over the course of a single revolution and the fourth varied over the course of 20 revolutions. During data reduction, the 48,800 samples per second time record was resampled to either 128 or 256 samples per revolution.

The unsteady pressure transducers utilized in this research effort measured the absolute pressure on the surface of the blade. They were calibrated before blade fabrication over a pressure range of 5 to 20 psia and a temperature range of 40°-140° F. These initial calibrations were done in a water bath calibration facility at the NASA Ames Calibration Laboratory to help choose the best transducers for installation into the HVAB blades. Only transducers verified to be within the manufacturer's maximum allowable specification of 0.5% of full-scale output, which corresponds to ±0.075 psi, were approved to be installed.

The selected transducers were then permanently installed into the internal structure of the SN004 blade. After blade fabrication was complete, a bag calibration was subsequently performed that enabled all the transducers to be verified and calibrated simultaneously. To perform the bag calibration, a vacuum bag, which was heat sealed at one end, was placed over the blade with the other end sealed against the outer mold line of the blade near the root using a flexible sealing compound. A vacuum pump was used to vary the pressure to several levels between atmospheric pressure and eight psia, during which data were acquired from the transducers. During this testing, 13 out of the 187 transducers were found to be non-responsive. The data from the functioning transducers were then utilized to establish the calibration coefficients for the subsequent data reduction. This bag calibration was done in-situ, utilizing the RDAS, cabling, and transducer power system that was used during the research testing. For the bag calibration, all but six of the transducers once again met the manufacturer's maximum allowable specification (±0.075 psi), with four of the six exhibiting a larger uncertainty range of ±0.088 psi and the last two having a reduced operating range and linearity after installation. No data from these last two transducers are presented here.

As a further check on the accuracy of the pressure data, a data point was acquired with the rotor stationary at the beginning and end of each run, and the measured data were compared against the barometric pressure recorded by the facility data system. If the measured pressure from a transducer was found to differ from measured barometric pressure by more than ±0.15 psi (1% FS) for both checks, the transducer was marked invalid for that run. If the transducer failed only one of the checks, the data quality from that transducer during the run was further investigated to see if it should be invalidated or not. The results of the two checks were also incorporated into the uncertainty quantification for each transducer.

Other Key Measurements

As mentioned earlier, each HVAB blade included a set of flap, chord, and torsion bending moment gages near the blade root for safety monitoring. In addition, one blade was designed with bending moment gage sets at three additional radial stations. All gages were calibrated prior to test and check-loaded prior to rotation. In addition, each of the four pitch link assemblies were gaged to measure control system loads. In particular, the pitch link axial load was determined from a gaged and calibrated pitch stud between the pitch link and cuff and included the effects of blade pitch angle (due to the kinematics of the joint).

Blade root angles were measured independently for each blade using angle transducers mounted at the blade cuff (Fig. 3). The transducer installation was designed to allow direct measurement of pitch, flap, and lag angles by installation at the relevant bearing locations. Calibrations were done in-place while mounted in the tunnel for best accuracy.

The rotor collective pitch was measured in two ways. The first measurement is derived from the fixed-system actuator positions as part of the pilot-station calibration. During this calibration, the actuators were positioned to provide specific pitch angles of the reference blade while ensuring the cyclic pitch was minimized. Thus, this measurement is consistent with a collective pitch derived from the reference blade only. The second collective pitch measurement can be determined using the root pitch measurements by averaging the mean values from all four blades. These four root measurements are not identical since the individual blades had slight pitch

adjustments made relative to the reference blade during initial track and balance runs.

In addition to the measurements of standard atmospheric conditions, local wind speed and direction were measured using a digital anemometer mounted near the tunnel centerline upstream of the model. The primary purpose of these measurements was to determine the nominal wind conditions prior to rotor start (to document whether the weather conditions outside the tunnel inlet induced a tunnel crossflow). The pre-run velocity measurements never exceeded 0.5 kt throughout the test program.

Independent Measurement Systems

This section describes the independent measurement systems used to provide blade deformations, flow transition locations, and wake geometry. The blade deformations were measured using photogrammetry, the flow transition locations were determined using thermography, and wake geometry was measured using shadowgraphy. Figure 6 provides a wide-angle view of the locations of the various system's equipment when installed in the NFAC. Detailed descriptions of each technique and how they were implemented in the NFAC are discussed below.

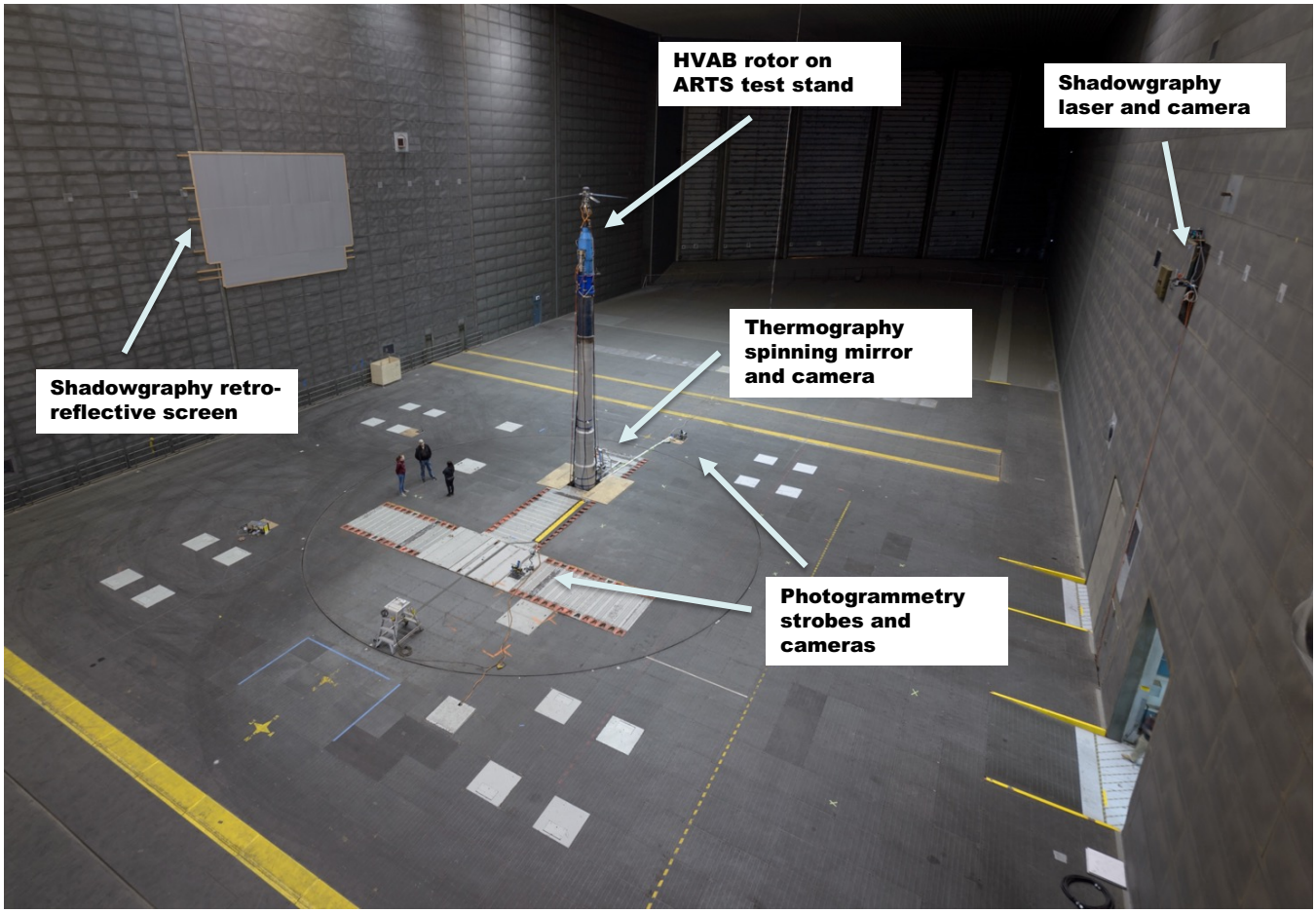

Figure 6. Wide-angle view showing locations of optical equipment in NFAC.

Photogrammetry for Blade Deformations

System Description

Deformations of the rotor blades—bending and elastic twist—were measured using stereo photogrammetry. Two synchronized and calibrated cameras were mounted on the floor of the test section equidistant upstream and downstream of the test stand (Figs. 1 and 6). The cameras acquired images of the rotor blades as they passed through $\psi = 270°$. Retroreflective targets were applied to the lower surfaces of all four blades (Fig. 7) and were illuminated by LED flash lamps co-located with the cameras. The 3-D spatial coordinates of all targets were computed from the 2-D image-plane coordinates of the targets in images and calibration coefficients from both cameras. Bending and elastic twist were computed by comparing the spatial coordinates of the targets in the loaded (rotor spinning) and unloaded (static) conditions after accounting for differences due to rigid-body displacements and rotations. The goal was to measure the elastic twist of the rotor blades to within 0.1°. This approach was very similar to that used to measure blade deformations of the PSP rotor in forward flight in the NASA Langley 14- by 22-Foot Wind Tunnel (Ref. 19). Prior to that test, photogrammetry had been used to measure deformation of a

full-scale rotor in forward flight in the 40- by 80-Foot Wind Tunnel at NASA Ames (Ref. 20).

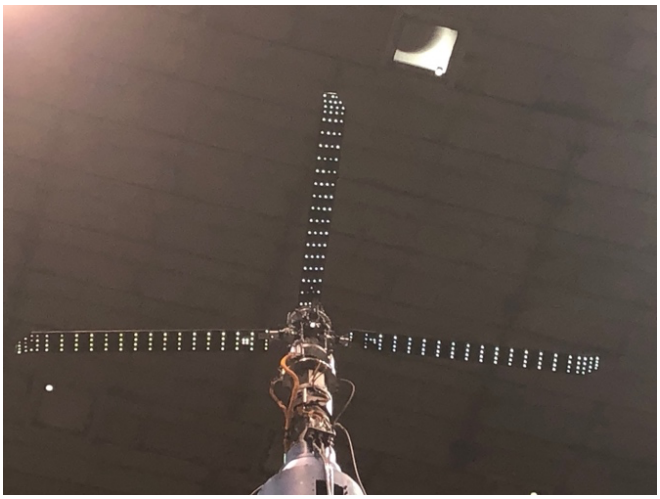

Figure 7. Retroreflective targets on rotor lower surface for photogrammetry measurements.

The cameras were Dalsa 12M Falcon digital (4096 x 3070 pixels, eight bits deep). They were placed 23 ft upstream (ψ=180° direction) and downstream (ψ=0° direction) of the test stand and were offset laterally from the test section centerline by the rotor radius. The angle between their optical axes was 60 degrees. Each camera was fitted with an f/2.8 180 mm focal length lens which resulted in spatial resolution of the rotor of about 63 pixels per inch. The rotor was illuminated by six LED flash lamps, three co-located with each camera. Four of the lamps were fitted with Fresnel lenses to concentrate the light at the measurement station.

The cameras and lamps were triggered by a once-per-rev signal that originated at the rotor shaft encoder. This signal was delayed by a Rotor Azimuth Synchronization Program (RASP) unit (Ref. 21) to place one of the four blades at the measurement station (ψ=270°). The output signal from the RASP was then input to a digital pulse generator which allowed separate control of the widths of the pulses presented to the cameras and lamps. These pulse widths set the integration time of the cameras (50 μs) and flash duration of the lamps (7 μs), respectively. The flash duration corresponded to a 0.061-in circumferential displacement of the rotor tip at 1250 RPM, or about 1% of the blade chord (5.45 in), resulting in a barely perceptible blur. Each camera recorded its images to a digital video recorder across fiber-optic cables. Image acquisition was controlled by a PC running IO Industries CoreView software. At each test point, images were acquired for 128 consecutive revolutions ("instances") as DAS data were also being acquired.

Eighty adhesive, retroreflective targets, punched from sheets of 3M 7610 material, were applied to the lower surface of each blade (on top of the black polyurethane paint used for thermography). The targets were ¼-in diameter and 0.005-in thick; they were arranged in chord-wise rows of four at each of 20 radial stations. The spatial coordinates of the targets in the blade coordinate system and with the blade supported to avoid bending (leading edge down, Fig. 8) were measured using a commercial photogrammetry system (V-STARS, Ref. 22). These coordinates were the unloaded reference against which loaded measurements were compared. At the reference collective condition (θ_0=0°), the angle of attack of the blade at r/R=0.75 was also 0°.

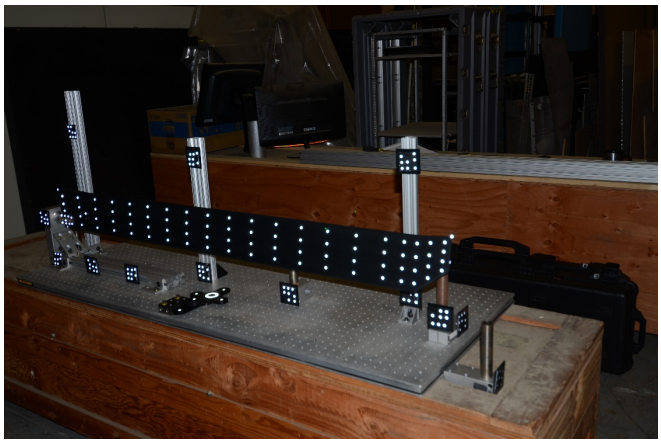

Figure 8. Setup for measuring unloaded blade coordinates by V-STARS.

The cameras were calibrated using a pinhole representation: each point in space was projected along a straight line through a pinhole lens and onto a flat image plane that was perpendicular to the optical axis (Refs. 23-24). As is customary, coefficients in the governing collinearity equations were separated into two groups: intrinsic parameters (scale factors, principal point, and skew) and extrinsic parameters (3-D position and point angles of the camera, "pose"). The intrinsic parameters were determined by Zhang's method (Ref. 25): after the cameras had been focused on the region of interest, images were acquired of a flat target board that was hand-held at many orientations relative to the camera at the same distance from the camera as the region of interest. Targets were located in all the images, and their 2-D pixel coordinates were used to compute intrinsic parameters.

The extrinsic coefficients of each camera were computed from an image of a flat target board that was supported horizontally in the rotor plane by a special fixture attached to the test stand (Fig. 9). The spatial coordinates of targets on the board were assumed to be known and established the coordinate system of the photogrammetry measurements. Beginning with a guess of the pose and knowing the intrinsic parameters, each target was projected into the image of each camera, and the projected pixel coordinates were compared to the actual coordinates measured in the images. The pose parameters were adjusted iteratively to minimize the root-mean-square re-projection errors of all targets.

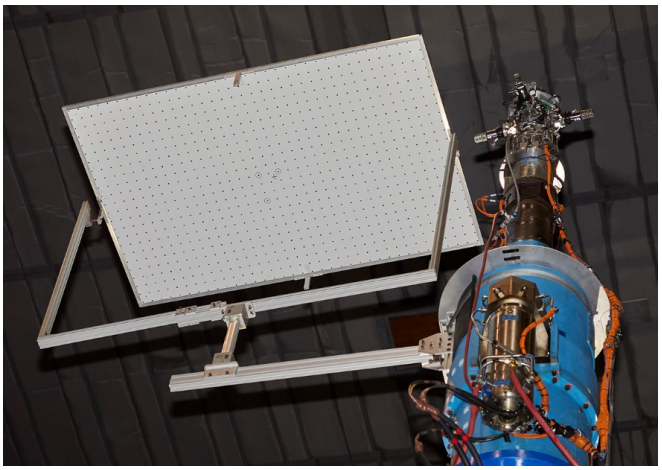

Figure 9. Photo of target board mounted to test stand for pose calibration.

Image Processing

Data reduction from the stereo photogrammetry images involved the following steps:

1. Locating targets in the images from both cameras
2. Computing the 3-D spatial coordinates of all targets at each instance
3. Computing six degrees-of-freedom rigid-body transformation between loaded and unloaded conditions
4. Applying the rigid-body transformation to 3-D coordinates of all targets, bringing them into blade reference coordinates
5. Computing bending and elastic twist from loaded and unloaded target 3-D coordinates in blade reference coordinates
6. Computing average and standard deviation of 128 instances

Target finding was a semi-automatic, two-step process. The first step was to define the approximate positions of all targets, either manually by point and click with the computer mouse, or automatically using target locations from a previous test point. The second step was to refine the approximate positions using an automatic target finder that searched within a rectangular window centered on the approximate location of each target. A third step—correcting incorrectly located targets—was also often necessary. Once the targets were located in the first image of a 128-image sequence, target finding in the following images was fully automatic.

The spatial coordinates of all targets were computed at each instance from the target pixel coordinates and calibration coefficients from both cameras (Ref. 26). The extrinsic calibration parameters were adjusted to minimize the root-mean squared re-projection error (Ref. 27). This optimization (bundle adjustment) had a very small effect on the solutions.

The rigid-body transformation between the loaded and unloaded conditions was computed at each instance by comparing the spatial coordinates of a set of rigid-body targets at both conditions and finding the rigid-body displacements and rotations that gave the best match. Defining rigid-body targets on a flexible rotor blade is problematic. Our baseline was to assume that the most inboard three rows of targets ($r/R \leq 0.25$) were rigidly connected. Then, to assess the sensitivity of the solutions to this assumption, the calculations were repeated using four ($r/R \leq 0.30$) and five ($r/R \leq 0.35$) rows as rigid. The unloaded spatial coordinates of the targets were those measured by V-STARS and were in the blade coordinate system. Knowing the position of the hinge (r=3.5 in), the angle of the rotor shaft (0°), and the azimuth of the measurement station (ψ=270°), the rigid-body rotations from tunnel (pose target board) to blade coordinates were resolved into pitch, flap, and lag angles.

Once the rigid-body transformation was computed, it was applied to all targets, taking them from the target-board to the blade coordinate system. After this transformation, differences between the loaded and unloaded spatial coordinates of all targets were assumed to be due to bending and elastic twist. Bending was displacement in the out-of-plane direction in blade coordinates, and the elastic twist at each radial station (computed from the four targets at each station) was rotation about the radial axis. Finally, the average and standard deviation of 128 instantaneous measurements were computed to represent a single data point.

Several "real-world" issues complicated the acquisition and analysis of the photogrammetry measurements. The most serious was loss of targets. In the two rows nearest the tip ($r/R \geq 0.95$), several targets on each blade often detached under centrifugal loading; and in the most inboard row ($r/R=0.15$), the brightness of two targets on each blade was often diminished due to oil contamination from the blade-cuff junction. Although lost targets were replaced before each run, they were often lost again shortly after resuming operation. A stronger adhesive was not used because the solvent necessary to remove the targets afterward would likely have damaged the underlying paint, which needed to be preserved for thermography. At rows where targets were missing, whether by detachment or contamination, the elastic twist computed from the remaining targets in that row (which sometimes was only two closely spaced targets) was often unreliable. Elastic twist measurements at these stations will therefore be omitted from the final database.

Thermography for Boundary Layer Transition

System Description

Boundary layer transition locations were measured using thermography, where the transition can be visualized using thermal imaging to detect temperature differences across the airfoil's surface. These differences are typically generated in one of two ways- passively, when the surface heats up more

in the turbulent region due to increased skin friction, or actively, after heating the surface a few degrees above the static temperature, when the surface cools down more in the turbulent region due to increased mixing with ambient air. The transition location is the same for each method, but the relative grayscale intensities in the image are opposite. The use of thermal imaging to visualize the heat signature of a boundary layer began with the first thermal imaging scanners of the late 1960s and was systematically applied for boundary layer evaluations of fixed airfoils in the mid 1980s by Quast (Ref. 28) and Carlomagno et al., (Ref. 29). It was only in the past decade, however, that thermal camera technology progressed sufficiently to allow for rotor blade transition characterization. Specifically, focal plane array cameras were developed that offered global shuttering and asynchronous frame rates, allowing for one-per-rev imaging regardless of rotor rpm. This new technology has subsequently been applied in several major rotor tests, both in wind tunnels (Refs. 30-31) and in flight (Refs. 32-33). Reference 34 discusses several aspects of the Differential Infrared Thermography (DIT) method (developed by the DLR Göttingen Helicopter Branch) for unsteady boundary layer situations, such as helicopter forward flight and pitching airfoils.

One method for imaging the surfaces of a rotating airfoil using a thermal camera was recently developed by Raffel and Heineck (Ref. 35). With this method, a radially aligned rotating mirror, with its spin axis closely aligned to the rotor spin axis and rotating at half the speed of the rotor, allows the virtual image of a blade to remain fixed on the camera sensor. This "freezing" of the image of the passing blade permits longer exposure times without incurring motion blur. The longer exposure brings the brightness to well above the noise floor of the camera and provides an image that can be used to detect the slight temperature difference between the turbulent and laminar areas of the airfoil.

The rotating-mirror method was implemented in this test, using a newly developed mirror tracking system and advanced thermal cameras, to image both the upper and lower HVAB blade surfaces. The mirror tracking system employed a National Instruments Compact RIO process logic controller (PLC) and Kollmorgen servo motors. Two 10- by 24-in rotating mirrors were built, each synchronized with the rotor by using "virtual" gearing of the servo motors to the rotor using the A, B, and Z signals from the RS-422 shaft encoder. These signals were used to set the gearing ratio to half the rotation speed of the rotor, to have the rotation reversible (upper and lower mirrors had to spin in the opposite direction), and to have the phase of the mirrors adjustable during operations. The PLC also produced a camera synchronization signal once per revolution whose phase was set using the encoder signals. Having both the camera synchronization and the mirrors controlled by the PLC permitted easy alignment of the mirror to the camera and to any of the four blades.

A FLIR X8501sc camera with a 1280 X 1024 Strained Layer Superlattice (SLS) sensor and fitted with a 100mm f2.3 lens was used in conjunction with each rotating mirror system. This camera is sensitive from 7.5 to 11 microns, which is near the peak of the Planck curve at room temperature. One mirror/camera assembly was installed in the attic of the wind tunnel to visualize the blade upper surface. The camera for this system peered through an anti-reflection coated Germanium window to prevent debris from falling into the rotor disk. The second assembly was mounted on the test section floor to visualize the lower blade surface. Figure 10 shows the installation of both systems (note the triangular-shaped Germanium window in the attic-mounted assembly). The cameras captured images when the blades were aligned with the tunnel centerline at the nominal 0° rotor azimuth position (see Fig. 6).

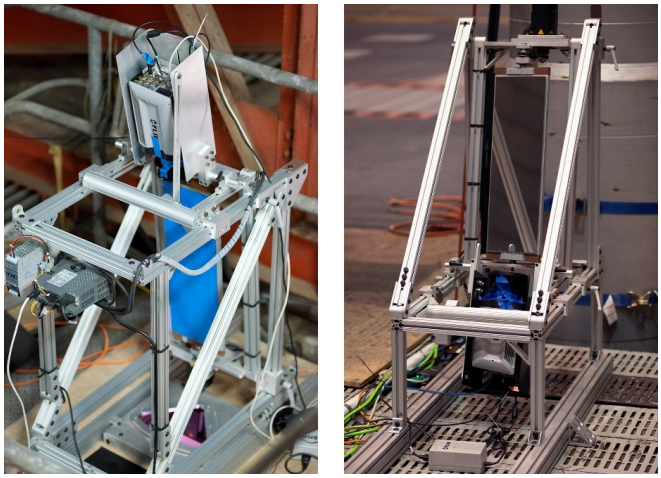

a) **b)**

Figure 10. Thermography system showing a) upper surface camera in the attic, b) lower surface camera on the test section floor.

The blades were coated with high-emissivity black polyurethane paint to improve thermal image quality, and then buffed to a surface roughness of less than 10 microinches (rms). Fiducial targets of gold ink (0.5 in diameter) were applied to all blade surfaces, spaced two inches apart and inset one inch from the leading and trailing edges. These low-emissivity targets were added to allow for blade image alignment and averaging during post-processing. Fifty images of each blade were acquired at each test condition during operations to allow for this averaging.

Early in the run schedule, a lubricant was found centrifugally seeping from the root of each blade. Subsequently, the blades were cleaned (with an aqueous detergent) prior to each run where thermography data were acquired to prevent confusion between the true transition heat signature and the variation of emissivity caused by the lubricant.

Image Processing

Each set of 50 images was stored as a FLIR-proprietary *.ats file, which concatenates each raw image and stores their thermal and grayscale data. Each image must be exported to a .tif file after rendering the 16-bit image data as a suitable 8-bit display. The images were rendered with as much pertinent grayscale data as practical. Further image processing was done to enhance the sharpness and contrast. The averaging process required that the fiducial targets in each image be located to subpixel accuracy. This was accomplished using the same target-finding and correction utility as was used for photogrammetry.

Additionally, a method for enhancing the contrast of the entire blade was developed. The images exhibited a large root-to-tip increase in brightness because of the increasing local Mach number and recovery temperature. In contrast, differences due to laminar and turbulent boundary layers were very small and were especially difficult to see inboard where the images were very dim. The contrast between laminar and turbulent regions was enhanced by first scaling the images radially to minimize the large root-to-tip brightness gradient. Then the image brightness levels were scaled between the relatively small difference in brightness between darker laminar and brighter turbulent regions. After this adjustment, contrast between laminar and turbulent regions was much greater and was approximately uniform from root to tip. Figure 11 shows a sample blade image through this workflow.

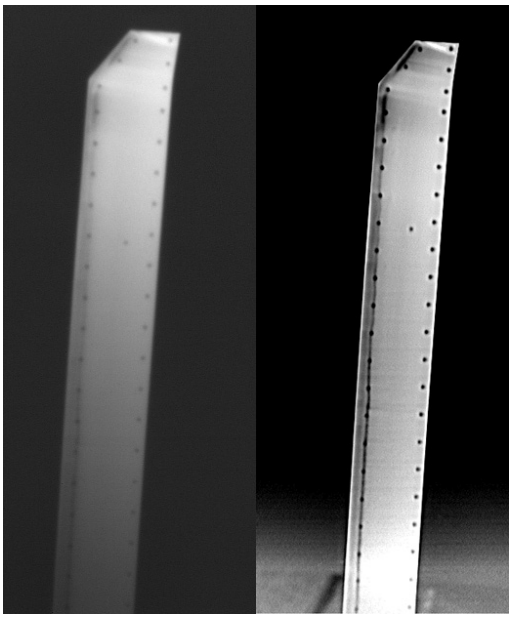

a) **b)**

Figure 11. Example of the effect of image processing steps for a single blade image. a) Sample of an image exported from the *.ats raw file and b) final image after sharpening, averaging, and applying the dual-slope contrast enhancement.

Transition of the boundary layer from laminar to turbulent was assumed to occur at the interface between dark laminar and brighter turbulent regions (Ref. 36). The chordwise position of this interface at each radial station was assumed to occur where the gradient of image brightness was greatest. An automatic algorithm was developed to locate this position at all radial stations, resulting in a line of transition from root to tip. The algorithm also found the leading and trailing edges of the blade at each station to compute the normalized position of transition from the leading edge (x/c). The normalized radial position (r/R) of each chordwise row was scaled from the known image and space coordinates of the tip and targets along the leading edge. Figure 12 shows how the transition line was determined from the chordwise grayscale intensity, its derivative showing the peak of the gradient, and the line of chordwise peaks of this gradient superimposed on an image.

Shadowgraphy for Wake Geometry

System Description

The rotor wake geometry was measured using shadowgraphy, where rotor tip vortices can be visualized due to density gradients in the vortices. The shadowgraphy (also referred to as shadowgraph) technique has been successfully used to capture images of the rotor wake geometry of small rotors in hover (Refs. 37-38) and a full-scale rotor in forward flight (Ref. 39). The measurement system includes a camera, a pulsed light source, and retroreflective screen. The rotor is positioned between the camera/light source and the retroreflective screen. As described in Norman and Light (Ref. 37), the light passes through the rotor tip vortices creating shadows on the screen, which are then captured by the camera. The shadows appear because the refractive index of the air is changed by the density gradient of the tip vortex.

For this experiment, a single camera shadowgraphy system was installed to provide both real-time viewing of the vortices and imagery that could be used to derive wake geometry. A 28- by 20-ft retroreflective background was created from seventeen 4- by 8-ft panels, which were mounted to the east wall of the tunnel, centered on the strut in the streamwise direction (Fig. 13a). A shelf was mounted 35 ft above the floor on the west wall, also abeam of the strut - see Fig. 13b. The camera was 1.75 inches upstream (toward the inlet) of the rotor center of rotation and mounted on a pedestal attached to the platform placing the camera at 39.1ft above the tunnel floor. The laser cone angle was adjusted to fill the retroreflective background. The camera and laser were configured using a 50/50 beam splitter, where the laser was projected through the beam splitter, while the camera viewed the region of interest of the reflected side. This configuration allowed the cone angle of the camera view to be co-located with the cone angle of the laser projection. The result eliminated a secondary shadow and assured that the scale of the vortices was not distorted.

The camera was a FLIR Machine Vision Oryx 25.4 Mpx camera fitted with a 45 mm tilt-shift lens. The camera sensor

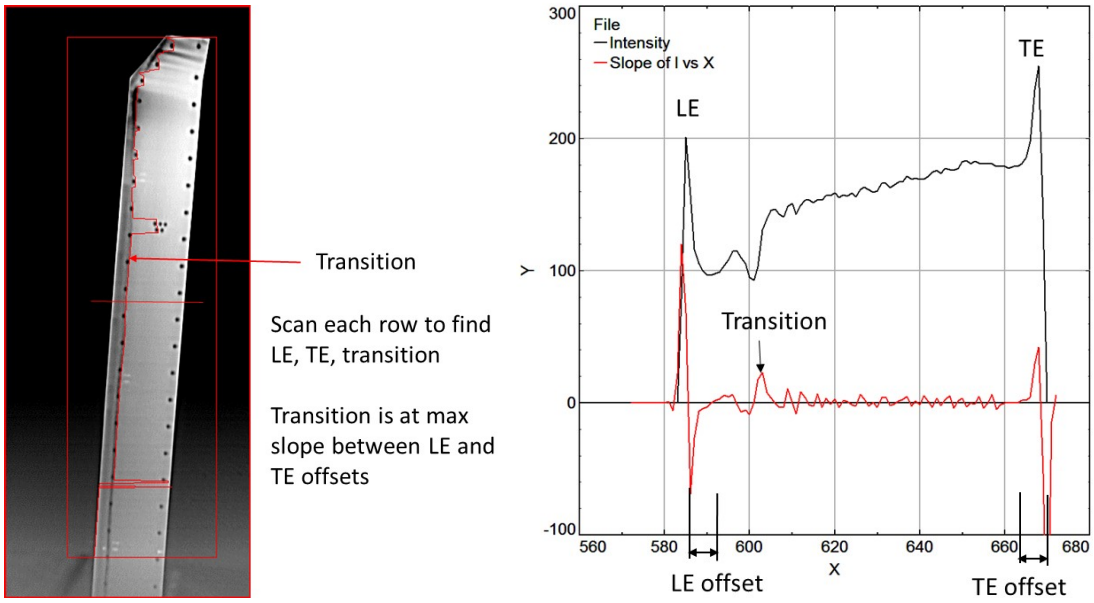

a) Trace of the transition line on the blade. **b) Intensity vs. Chord and Derivative of Intensity vs. Chord.**

Figure 12. Plots showing the derivation of the chordwise location of the transition.

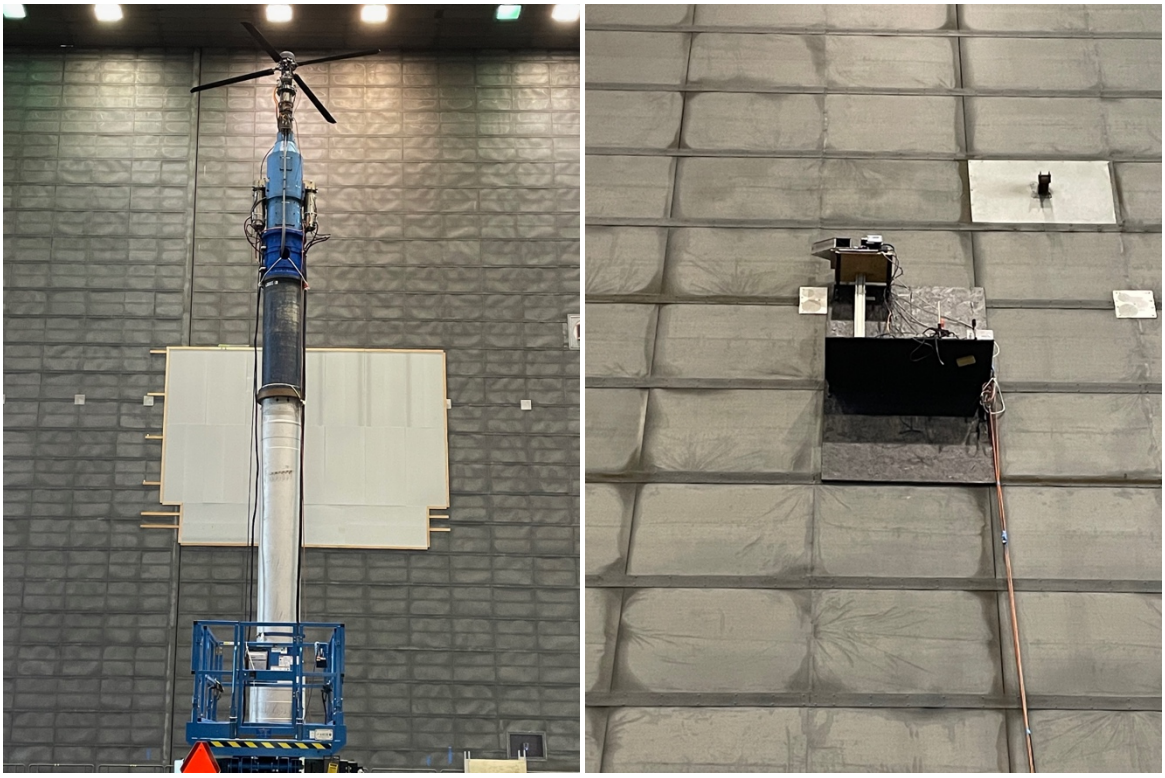

a) Retroreflective screen mounted on east wall. **b) Camera+laser platform, west wall.**

Figure 13. Shadowgraphy system installation in the 80- by 120-Ft Wind Tunnel test section.

remained vertical to prevent a perspective shift, and the shifting mechanism of the lens maintained image-plane/lens-plane verticality while allowing for the region of interest to be properly framed. An LED light source was initially used but was replaced with a Cavilux Smart HF Diode pulsed laser (Class 3B) with 640 nm wavelength. Compared to the LED source, the laser light produced much crisper images. The Cavilux was operated at 2 μs per pulse and was driven by the RASP. The RASP generated a delayed one-per-rev pulse train. A parametric study was made to determine if the full resolution of the camera sensor was required or if 2x2 binning of the pixels, where four adjacent pixel values are added and rendered as a single pixel, would be appropriate. The advantages of binning are increased quantum efficiency, reduced image noise, and more efficient data acquisition. The detection of the vortices with image processing required that they are represented in at least 5x5 pixels. Figure 14 is an enlarged view of a 90° wake-age vortex in a sample image; the early wake age vortex is defined by much more than five pixels, confirming the 2x2 binning to be acceptable. Each image size is 2300 pixels x 2656 pixels (vertical x horizontal).

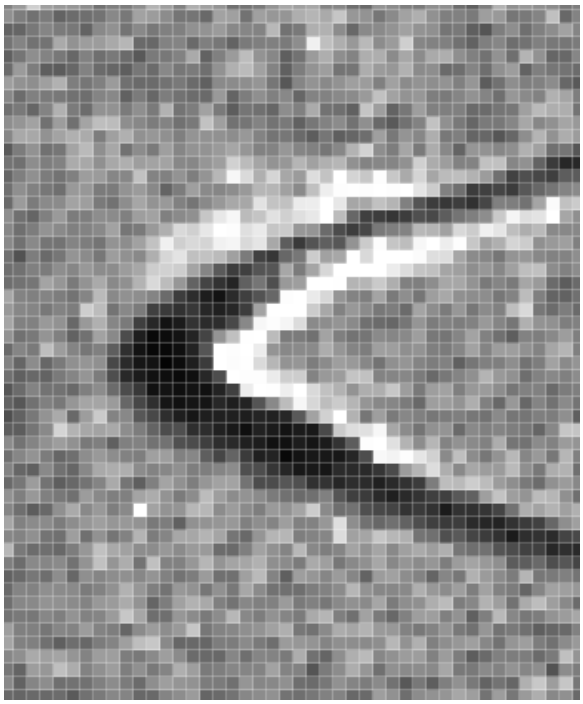

Figure 14. Enlarged view of small region of a sample 2x2 binned shadowgraphy image showing a blade tip and a 90° wake age vortex. Note the cross-section of the vortex is 12-15 pixels.

The shadowgraphy system was operated from the wind tunnel control room. The software SpinView 2.4.0.144 was used to select camera settings and acquire images at a specified rate controlled by the RASP. The RASP received the 1/rev signal from the rotor and divided the signal to drive the laser and trigger the camera acquisition at specific blade azimuth positions. For the sample shadowgraphy results shown in this paper for M_{tip}=0.65 and θ_0=12°, the RASP was used to acquire images from 0-345° azimuth at intervals of 15°, at an image acquisition rate of one image every 12 revolutions. The resultant rate of 1.74 Hz (rotor speed of 1250 rpm (20.83 Hz) divided by 12) was a trade-off between the time needed to acquire 100 images at 24 (360/15) azimuth positions and the desire to keep the test run to a reasonable duration.

Figure 15 shows a typical shadowgraphy image. Notable features are four tip-vortex trajectories on each side of the rotor, with the tip vortices nearest the rotor blades being more visible due to the stronger density gradient of these early wake age tip vortices.

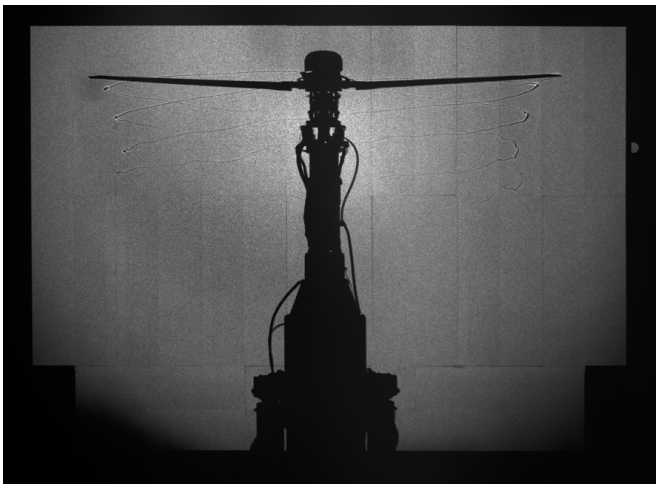

Figure 15. Typical shadowgraphy image, M_{tip}=0.65 and θ_0=12°.

Image Processing

The goal of the image processing was to characterize the radial contraction and axial positions of the vortices - with respect to the blade tips - as a function of wake azimuth angle (or wake age). The challenge was to extract only the outermost extent of the wake trajectory; for example, in Fig. 15, four tip vortices are visible on each side of the wake. The vortices move– due to flow environment and blade motion – from one image to the next image.

Manual extraction of the tip vortex location using a point-and-click digitizer is always an option, but not practical for processing thousands of images. Instead, a technique was developed using a grayscale gradient (GSG) approach.

As described earlier, Fig. 14 represents a section of a typical shadowgraphy image. The image is in grayscale, meaning that each pixel has a value between 0 (black) and 255 (white). The GSG method interrogates the image by marching along each row of the image search area and for each pixel location, computes a grayscale gradient value G(i,j) defined in Eqn. (1),

$$G(i,j) = \text{abs}(g(i,j) - g(i-1,j)) + \text{abs}(g(i+1,j)-g(i,j)) \qquad \text{Eqn. (1)}$$

where g is the pixel grayscale value and (i,j) represent the (column,row) coordinate of the image. G(i,j) will be largest near the location of the outermost extent of the tip vortex trajectory, as shown Fig. 16 with a row outlined in red and the high-gradient region circled in yellow.

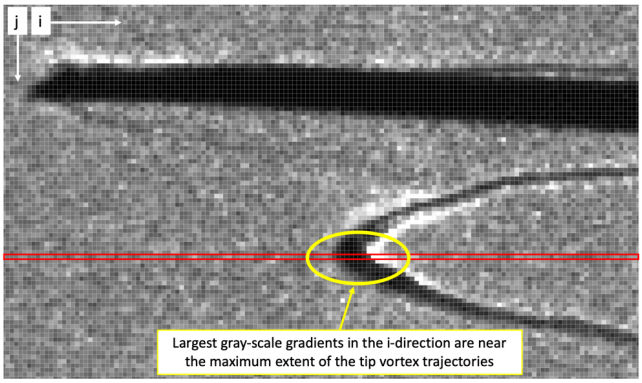

Figure 16. Implementation of computing grayscale gradients for a row of pixels.

Figure 17 shows a sample result of implementing the GSG method for the left side of a shadowgraphy image, such as Fig. 15. The symbols shown in the plot identify pixel locations that meet a user-specified threshold for the value of G(i,j). The threshold value was determined iteratively to eliminate outliers and low values of GSG. Since the general locations of the tip vortices were known, a rectangular region large enough to capture the clusters shown in Fig. 17 was defined for each of the eight vortices – four on each side of the wake. No more than four blade passages of the wake were observed and sometimes, as in Fig. 17, the fourth vortex was not identified by the GSG method. Within each of the eight rectangular regions, centroids (x- or i-direction and y- or j-direction) based on the value of G(i,j) and the pixel location (i,j) were computed. In Fig. 17, the centroid is identified as a solid symbol within the cluster of open symbols.

Further data processing is required to convert the vortex positions to blade coordinates (z/R and r/R) and to determine the wake ages of each vortex. Conversion to blade coordinates requires knowledge of the center of rotation as well as the relative location of the blade tips in pixel space. The center of rotor rotation was determined using two approaches; the results differed by approximately two pixels, so the results were averaged. The blade tip location was determined by using the same GSG approach described above, this time the interrogated regions of the image were the two blade tips for the blade azimuth settings of 0, 90, 180, 270, 360 degrees and 15, 105, 195, 285 degrees. From these tip locations, the minimum and maximum pixel locations in the radial direction were determined and a tip-to-tip pixel value was defined as the rotor diameter. The radial locations of the blade tip for the left and right side of the image were then determined from the rotor diameter and the center of rotation. The vertical location of the tip in the left side of the image was approximately 0.84 inches lower than the tip shown in the right side of the image.

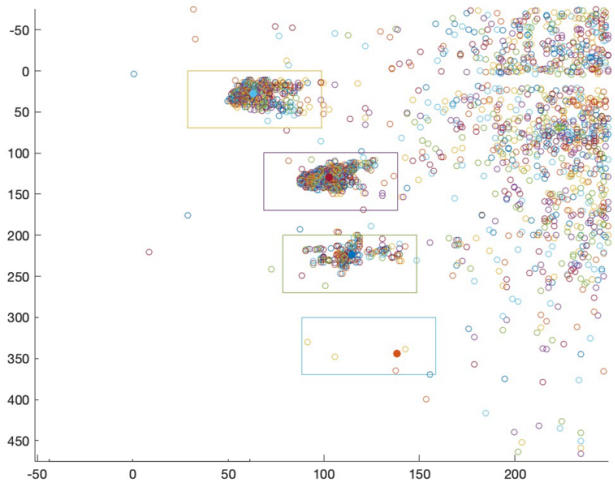

Figure 17. Pixel locations with high grayscale gradient (G(i,j)) values are plotted. The three clusters of symbols represent tip vortex locations. The solid symbol is the centroid computed from the G(i,j) values within the rectangles.

The determination of wake age starts with the rotor azimuth at which the shadowgraphy laser is triggered and then adjusted to account for the blade lag and the assumption that the tip vortex is formed at the blade trailing edge. The average blade lag of all four blades is determined from the measured root lag data acquired at each condition (-3.20° for the M_{tip}=0.65 and θ_0 = 12° condition). The angle between the quarter-chord line and the blade trailing edge, referenced from the lag hinge, is 3.72° in the lag direction. The largest adjustment is due to the camera seeing a foreshortened view of the rotor disk edge because the camera is not infinitely far from the rotor – see Fig. 18. This view results in corrections of -5.38° and 5.38° that are applied to the azimuth location of vortices on the left and right sides, respectively, of the image.

TEST CONFIGURATIONS AND ACQUIRED DATA

The research data described above were acquired for three distinct blades-on configurations: 1) standard HVAB blades with natural boundary layer transition, 2) standard HVAB blades with forced boundary layer transition, and 3) pressure blade with natural boundary layer transition. Detailed descriptions of each configuration, with the resultant research test conditions and types of data acquired, are provided below and listed in Table 3.

Standard Blades – Natural Transition

The first configuration utilized the three sparsely instrumented HVAB blades (SN001, SN002, SN003) along with the more highly instrumented strain-gaged blade (SN005). As shown in Table 3, this was the configuration for which most of the blade deformation, transition, and wake geometry data were acquired. Testing in this configuration

was separated into three phases. The objective of the first phase was to acquire blade deformation data for three rotor RPM's (1160, 1250, and 1310) over a range of collectives/thrusts. RPM (rather than M_{tip}) set points were used for this phase since dimensional loads directly impact the blade deformation. Note also that although the performance data (especially torque) from this testing were affected by the installation of the retroreflective targets on the blade lower surfaces, the measured deformation data are not expected to be significantly affected and thus can be used to compare with aeroelastic predictions.

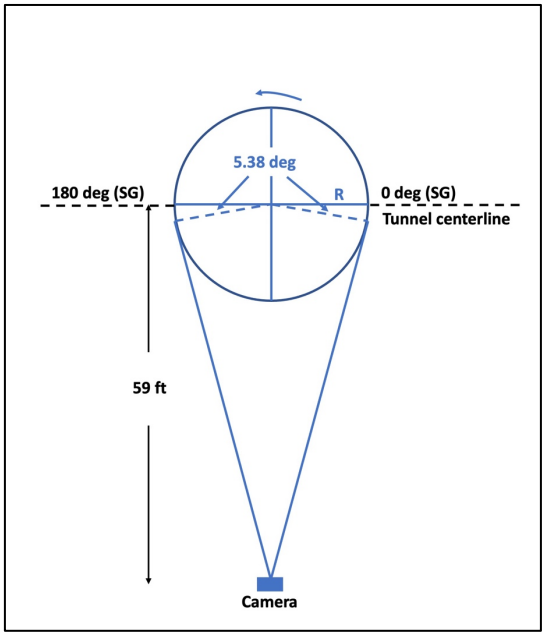

Figure 18. Planview of shadowgraphy camera view of rotor disk and resulting correction (5.38°) to wake age.

The objective of the second phase of testing was to acquire performance and transition data for closely spaced collective settings at three tip Mach numbers (0.60, 0.65, and 0.675). These data can be used to evaluate the effects of smaller collective changes on transition locations (and subsequently performance), especially at lower collectives. The objective of the third phase was to acquire simultaneous performance, transition, and wake geometry data for a select number of collective settings at each of the three tip Mach numbers. Collective settings for this phase were limited to the higher values ($\theta_0 \geq 8°$), when the shadowgraphy vortices were most visible.

Standard Blades – Forced Transition

The second configuration utilized the same blades as for natural transition, but with trip dots applied on the leading edges to force transition to turbulent flow. The objective of this configuration was to provide performance data for validation of analyses that do not model transition.

Table 3. Test Configurations and Conditions

Performance (P), Photogrammetry (PG), Thermography (TG), Shadowgraphy (SG), Airloads (A)

Config	M_{tip} or RPM	θ_0	Key Meas	Primary Objective
Standard blades, natural transition	1160, 1250, 1310 RPM	4, 6, 8, 10, 11, 12, 13, 14	P, PG	Blade deformation
	0.60, 0.65, 0.675	4 to 15 1 deg incr	P, TG	Performance and transition
	0.60, 0.65, 0.675	8, 10, 12, 14	P, TG SG	Wake geometry
Standard blades, forced transition	0.60, 0.65, 0.675	4 to 15 1 deg incr	P, TG	Fully tripped
	0.60, 0.65, 0.675	4, 6, 8, 10, 12, 14	P, TG	Tripped lower surface only
Pressure blade	0.60	4 to 12 1 deg incr	P, TG SG, A	Blade Airloads
	0.65	4, 6, 8, 10, 11, 12, 13	P, TG SG, A	Blade Airloads

To accomplish this, trip dots were applied to the upper and lower surfaces of the blades in a manner similar to that used during previous PSP blade testing (Ref. 13). A chordwise trip location of x/c=0.05 was chosen for both surfaces based on these earlier results. The trip dots used are commercially available and have a diameter of 0.050 inches and a spacing of 0.1 inches center to center. A variety of heights are available, from 1.1 to 16.0 mils (0.0011 to 0.016 in).

To avoid overtripping the boundary layer and introducing excess drag, an initial study was performed to determine the trip dot height needed to force transition at x/c=0.05. Different heights (ranging from 2 to 8 mils) were applied to each blade on both the upper and lower surfaces, and thermography data were collected over a variety of conditions. The data demonstrated that transition was successfully forced using dots with a height of 3.5 mils on both the upper and lower surface for all conditions. This height dot was then applied to all blade surfaces, with a sample application shown in Fig. 19. Forced transition was then studied at the three primary M_{tip} values, with both performance and thermography data collected.

Following this initial testing, the trip dots on the upper surface of each blade were removed so that transition was forced only on the lower surface. The goal of this configuration was to study if the performance would match the fully forced case at

high collective (since the upper surface was fully turbulent even during natural transition testing). Performance and thermography data were collected at all collectives listed in Table 3 for M_{tip}=0.65, but only at the three highest collectives for the other two M_{tip} conditions.

Pressure Blade – Natural Transition

The third configuration replaced one of the sparsely instrumented HVAB blades (SN003) with the highly instrumented pressure blade described earlier (SN004). The objective for this testing was to acquire performance, airloads, transition, and wake geometry data over the full range of collective values and tip Mach numbers. Ultimately, due to hardware issues, data were limited to a reduced set of collectives for M_{tip} values of 0.60 and 0.65 as shown in Table 3.

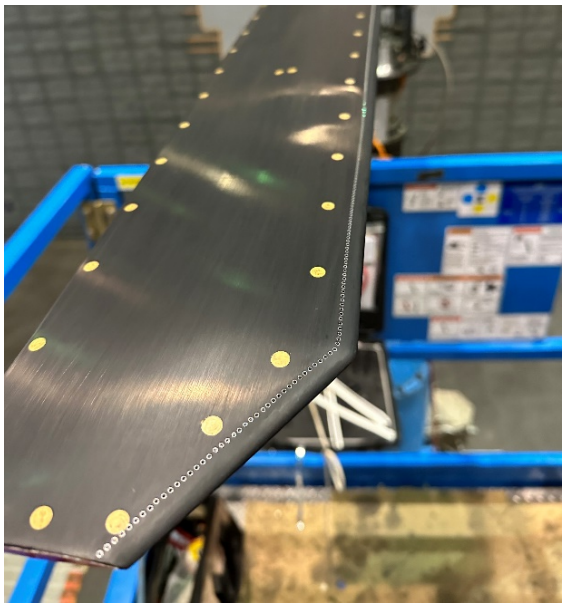

Figure 19. Trip dot application on upper surface of blade.

During testing of this configuration, the measured rotor performance was reduced compared to data acquired with the standard blades (up to 2 counts of FM at lower collectives). Thermography data suggests these differences can be attributed to additional turbulent flow on the blades caused by the pressure transducers on the pressure blade as well as some residue left on the other blades from the trip-dot testing. Fortunately, these issues should have a much smaller effect on the rotor thrust than the torque (for a given collective) and the resulting airloads data should remain valid.

PRE-RESEARCH OBSERVATIONS AND EFFECT ON OPERATIONS

Prior to the start of research data acquisition, a significant amount of blades-on checkout testing was conducted to evaluate the quality and repeatability of the primary measurements and to determine the best operating procedures. This testing identified two major areas to address: balance thermal drift and the effects of recirculation. A review of these areas and their effect on operations is provided below.

Balance Thermal Drift

Initial running demonstrated that the mean balance thrust loads would drift between the beginning and end of a run, especially after a cold start. Thermal expansion of test stand components and its effect on balance measurements is a known testing concern; the ARTS uses an instrumented flex-coupler to account for this. Even with this additional measurement, however, the drift of the total thrust was found to be too high to meet the research objectives. This was ultimately addressed by requiring a pre-heat run immediately prior to each research run. During this pre-heat run, the rotor was spun up to full RPM at moderate torque values to heat up the ARTS balance and rotating systems. Running until the flex-coupler thrust measurement leveled out was sufficient to minimize drift during the following run. These pre-heat runs typically lasted 30 to 60 minutes, depending on atmospheric conditions.

Even with the pre-heat runs, some small thermal drift of both the thrust and torque measurements was seen during most research runs. Although relatively small (maximum of 5 lbf of thrust and 2 ft-lbf of torque), application of a simple drift correction during post-processing improved data quality. This correction assumes the drift is linear over the elapsed time of the run and corrects each data point as a function of time. Application of this correction resulted in greater repeatability between runs.

Effects of Recirculation

It was also observed during initial running that rotor thrust and torque measurements acquired over the 128-rev data points showed significant variation from point to point. Follow-on data acquisition over a 10-min period showed thrust and torque fluctuations occurring together at seemingly random intervals for varied lengths of time (from 5-30 s). Unsteady recirculation was suspected and qualitatively confirmed using tufts attached near the tunnel side wall. The tuft movement progressed from hanging straight down to straight up as the rotor thrust was increased, indicating the rotor outwash along the tunnel floor was turned upwards and climbed the tunnel wall, presumably, to be ingested by the rotor. The unsteady nature of the recirculation was indicated by the oscillatory motion of the tuft. The presence of unsteady flow was later confirmed from data acquired by the photogrammetry and shadowgraphy systems. Both systems showed long-period variability of the blade tip and/or vortex positions.

To account for these unsteady effects and ensure the desired mean data accuracies, subsequent research runs included acquisition of multiple data points over a 5-to-10-min period. The number of points and the period over which data were

acquired were dependent on the test configuration and type of research data being acquired. Ultimately, the repeat points were averaged to provide the best mean data.

For the performance and airloads measurements, acquiring 10 data points (each data point at 256 samples/rev for 128 revs) at each condition over a 5-min period was sufficient to provide the desired accuracy for FM when averaged (0.005, 95% confidence interval). For photogrammetry, five sets of data (each set consisting of 128 image pairs acquired over consecutive revolutions) were acquired over a 2.5-min period for each of the four blades. For shadowgraphy, 100 images were acquired over a 1-min period for every wake age (15° increments). The thermography images showed minimal effects due to the recirculation (the blade temperatures change very slowly), so 50 images were acquired over 50 consecutive revs for each blade surface (nominally a 2.5 sec period).

SAMPLE RESULTS

Research data acquisition (following the operating procedures identified above) has been completed for the three configurations outlined in Table 3. Data reduction is underway with the data workflow finalized for most of the key measurements. In the following sections, representative data from each measurement group is presented and discussed. For blade transition locations, wake geometry, and blade pressure measurements, the discussion is focused primarily on one test condition, M_{tip} = 0.65 (RPM = 1250) and θ_0 = 12° (C_T/σ = 0.0961). For the rotor performance and blade deformation measurements, results from other test conditions are also presented.

Rotor Performance

Figure 20 shows the acquired rotor performance data (FM vs. C_T/σ) for a typical collective sweep at M_{tip}=0.65 for the standard blade configuration with natural transition. Each data point represents the average of data acquired at 256 samples/rev for 128 revs and is corrected for balance thermal drift. The variability due to recirculation is evident when comparing the values for each of the ten data points acquired at the same condition (data acquired over a 5-min period). The character of the data scatter (not purely in the C_T/σ or FM directions) is consistent with the fact that rotor thrust is a component of both parameters. The average of the ten data points at each condition is also shown in the figure and demonstrates the effectiveness of using the operational procedures discussed above (providing a 95% confidence interval for FM= ±0.005).

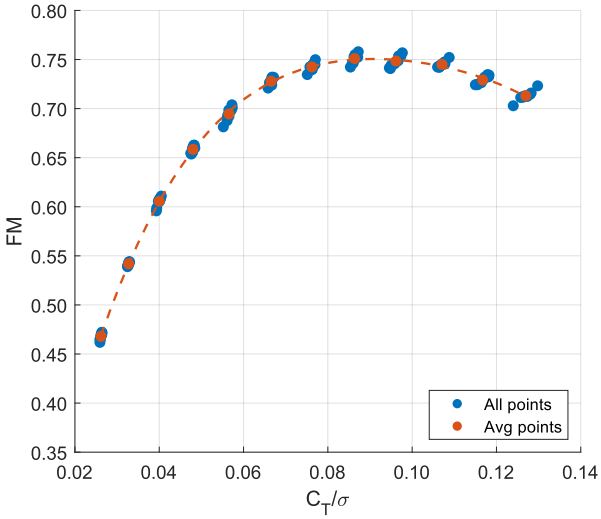

Figure 20. Rotor performance with natural transition at M_{tip}=0.65. Includes data from individual data points as well as averages.

Figure 21 compares the final averaged performance at M_{tip}=0.65 with data at M_{tip}=0.60 and 0.675. Reduced rotor performance is apparent at higher values of thrust as M_{tip} is increased. These types of data are critical for comparison with analytical predictions and the high-quality performance measurements from this test (in conjunction with the transition, deformation, wake geometry, and airloads) should allow for a full validation of analytical capabilities.

Figure 22 shows the effects of forcing transition (with trip dots) on the average rotor performance at M_{tip}=0.65. Data are presented for the natural transition, the fully forced transition, and the lower surface forced transition cases. As expected, there are significant differences in performance between the natural and forced transition cases (similar to the results of Ref. 13). On average, the performance drops by 4.9 counts in the fully forced case, with the difference decreasing as C_T/σ increases. For the lower surface forced case, the performance falls in between the other two cases, being closer to the natural transition results at lower thrusts and to the fully forced transition case at higher thrusts. This is consistent with the thermography results for these conditions, where the lower surface is naturally more turbulent and the upper surface is more laminar at low thrusts, and vice versa at higher thrusts. These data are expected to be useful, in conjunction with the thermography data, to evaluate analytical tools with no transition modeling.

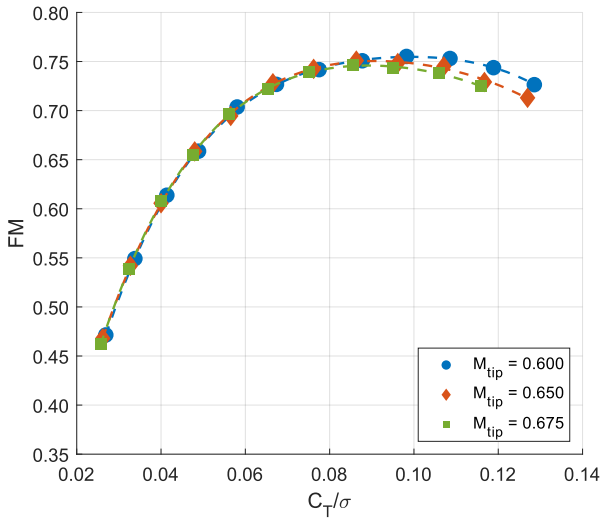

Figure 21. Rotor performance with natural transition at three M_{tip} values.

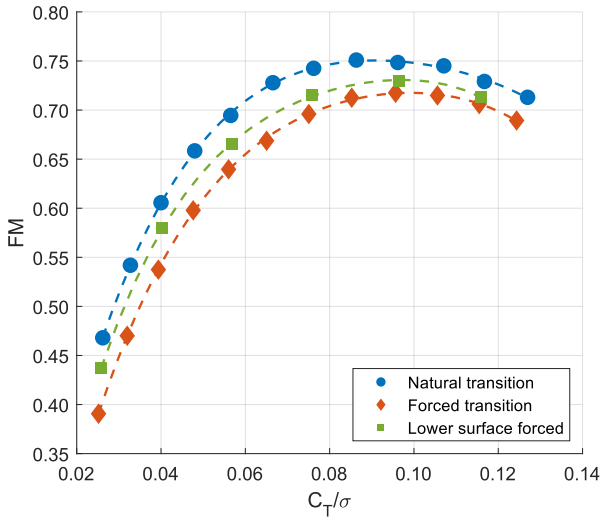

Figure 22. Rotor performance with natural, fully forced, and lower surface forced transition at M_{tip}=0.65.

As discussed previously, the key contributors to performance uncertainty include both the balance measurement accuracy (balance calibration accuracy and thermal drift) as well as the data scatter due to flow recirculation. With the known calibration accuracy (1 lbf thrust and 1 ft-lbf torque) and estimated balance drift error (1 lbf thrust and 0.5 ft-lbf torque after the drift correction), an uncertainty estimate of FM=±0.002 can be computed (due only to the balance measurements). This is significantly smaller than the effects of data scatter from the balance measurements (95% confidence interval for FM= ±0.005) and suggests the variation in flow conditions is the primary driver of uncertainty.

Blade Deformations

Representative blade bending and elastic twist measurements are presented in this section for the rotor at RPM = 1250 (M_{tip}=0.65) and θ_0 = 12°. Typical images of one blade (SN002) from both photogrammetry cameras are shown in Fig. 23. The inboard three rows of targets that were used as baseline rigid-body targets are indicated by the yellow circles. Missing targets are circled in red: one each in the two most outboard rows that became detached and two in the most inboard row that were contaminated by oil. Figures 24 and 25 show the resultant bending and elastic twist measurements versus normalized radius (r/R) for a single blade (SN002). Each measurement is the average of 128 instances, and measurements were repeated five times in succession over a 2.5-min period. Error bars indicate ± one standard deviation of the 128 instances. Bending is defined along the elastic axis (x/c = 0.25) and was interpolated from measurements at the targets. Displacement at the tip due to out-of-plane bending (DZ) varied between 0.7 and 1.0 inches (Fig. 24). Elastic twist measurements near the tip (Fig. 25) repeated within 0.5° (between -1.8° and -2.3°). Each set of elastic twist measurements has been fitted with a cubic polynomial. Measurements at the two most outboard rows (r/R = 0.97 and 0.99), where targets were missing, are not shown. Elastic twist becomes increasingly negative (nose down) from hub to tip, approaching a maximum negative amplitude of -2.3° at r/R=0.95. An anomalous data point at r/R = 0.25 was also quite repeatable and deviated from the cubic fits by about 0.1°. The reason for this anomaly is unknown: all targets at that station were present and accurately located in the images from both cameras.

In Figs. 26 and 27, bending and elastic twist averaged over the five repeated data points are shown for each of the four blades at the same test condition (RPM = 1250, θ_0 = 12°). The error bars indicate standard deviation of the five repeated measurements of each blade. The average tip displacements of the four blades agree to within about 0.1 inches, and the variations of bending with normalized radius are quite smooth. The elastic twist measurements are much less smooth and have been fitted with cubic polynomials. Measurements are not shown at the two outboard stations of blades SN002 and SN001 because of missing targets. These elastic twist measurements suggest the blades may not be structurally identical, but the maximum difference is still less than 0.5°.

The bending and elastic twist of all four blades can then be averaged together to provide mean blade deformation data for comparisons with analysis. Examples of this approach are shown in Figs. 28 and 29 for a range of collective pitch angles between 4° and 13°. There is a monotonic increase in bending as collective pitch increases, whereas elastic twist becomes increasingly negative. Note that the twist anomaly at r/R=0.25 appears even in these averages.

The uncertainty of the photogrammetry measurements was estimated in several ways. Each measurement was the least-squares solution to a set of four equations and three unknowns

(x, y, and z) and thus was not exact. The magnitude of the residual error can be interpreted as standard deviations of the measurement in the x, y, and z directions (Refs. 23, 26). For a typical case, the standard deviation in the z direction was between 0.03 and 0.06 inches. The uncertainty of each measurement was also estimated by placing in the region of interest an object with two targets separated by a known distance. The separation of the targets in the z direction measured by photogrammetry agreed with the known separation to within 0.058 inches. Finally, to address the uncertainty due to the assumption that the inboard three rows of targets were rigidly connected, the solutions were repeated using first four and then five rows as rigid-body targets. Increasing rigid-body targets from three to five rows reduced the computed bending at the tip by about 0.1 inches and reduced the absolute magnitude of the computed elastic twist by about 0.1°.

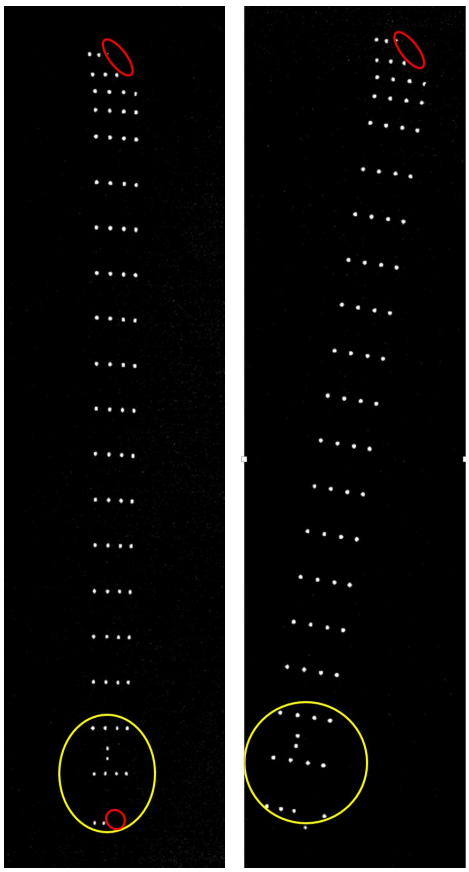

Figure 23. Typical images from upstream (left) and downstream (right) photogrammetry cameras (blade SN002, RPM=1250, θ_0=12°). Blade tip is at the top and rotation is clockwise as seen from below. Baseline rigid-body targets are indicated by yellow ellipses, missing targets by red ellipses.

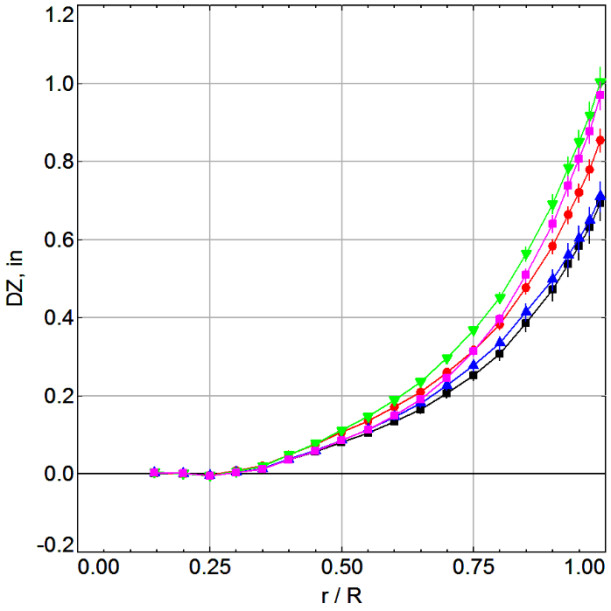

Figure 24. Sample photogrammetry data showing repeated bending measurements along elastic axis vs. radius (θ_0=12°, RPM=1250, blade SN002).

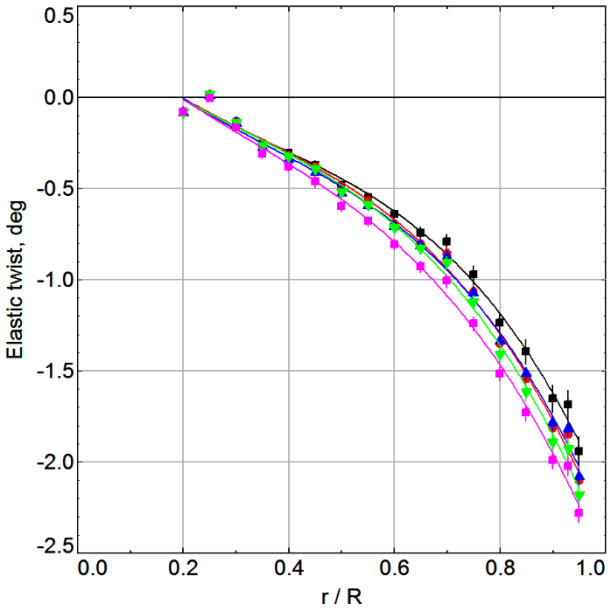

Figure 25. Sample photogrammetry data showing repeated elastic twist measurements vs. radius (θ_0=12°, RPM=1250, blade SN002).

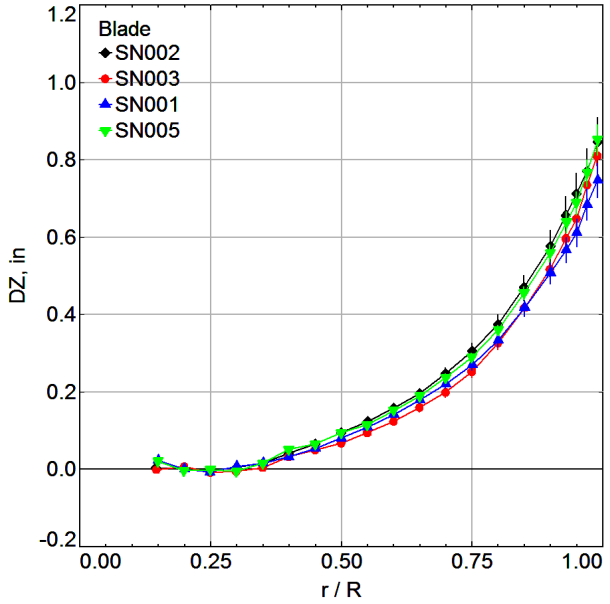

Figure 26. Sample photogrammetry data comparing average bending measurements along elastic axis of four blades vs. radius (θ_0=12°, RPM=1250).

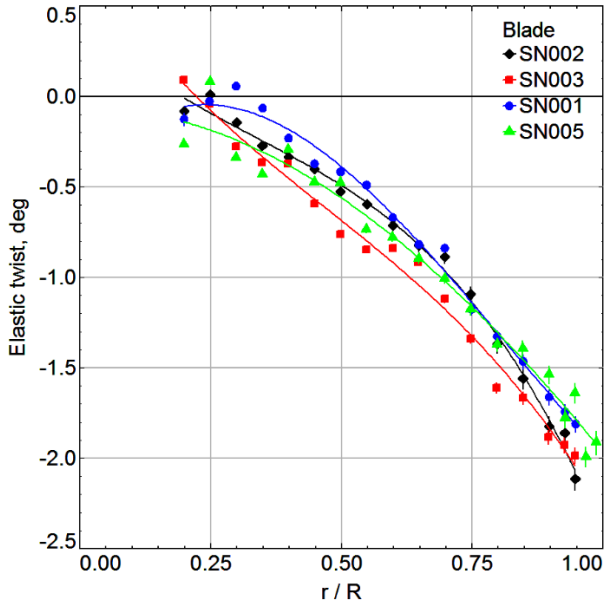

Figure 27. Sample photogrammetry data comparing average elastic twist measurements of four blades vs. radius (θ_0=12°, RPM=1250).

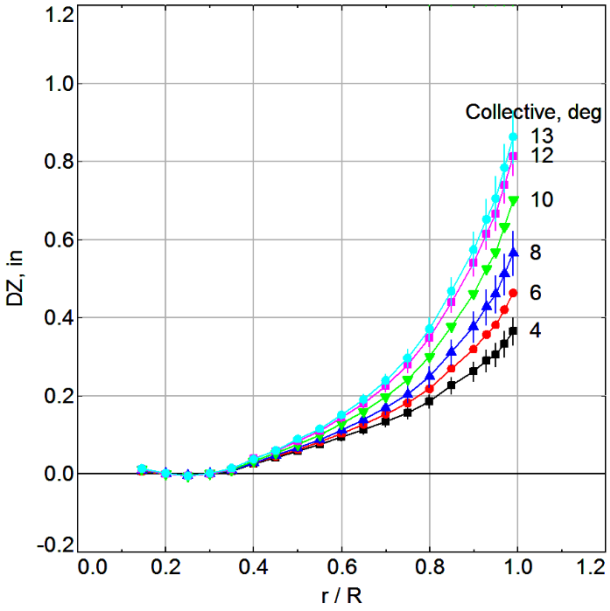

Figure 28. Sample photogrammetry data showing effect of collective pitch on average bending measurements along elastic axis of four blades vs. radius (θ_0=4°-13°, RPM=1250).

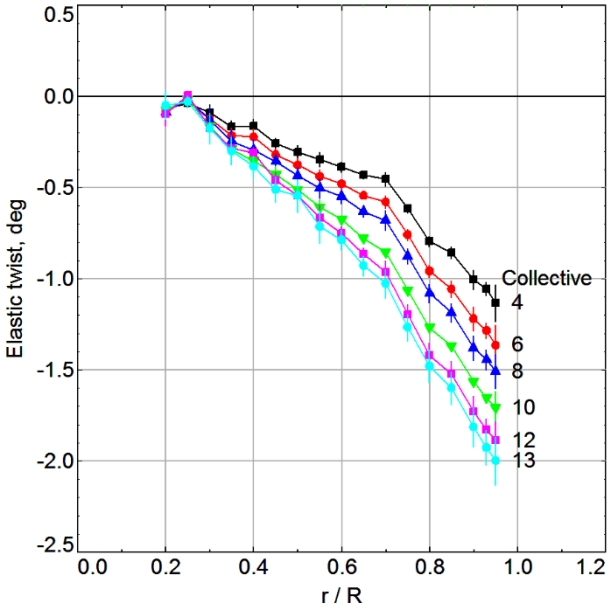

Figure 29. Sample photogrammetry data showing effect of collective pitch on average elastic twist measurements of four blades vs. radius (θ_0=4°-13°, RPM=1250).

Blade Transition Locations

Figures 30 and 31 show thermal images of the upper and lower surfaces for each blade at M_{tip}=0.65 and θ_0=12°. Each image has gone through the thermography image processing described earlier: sharpening each of 50 images acquired at the same condition, aligning and averaging the 50 images, and applying the dual-slope contrast enhancement.

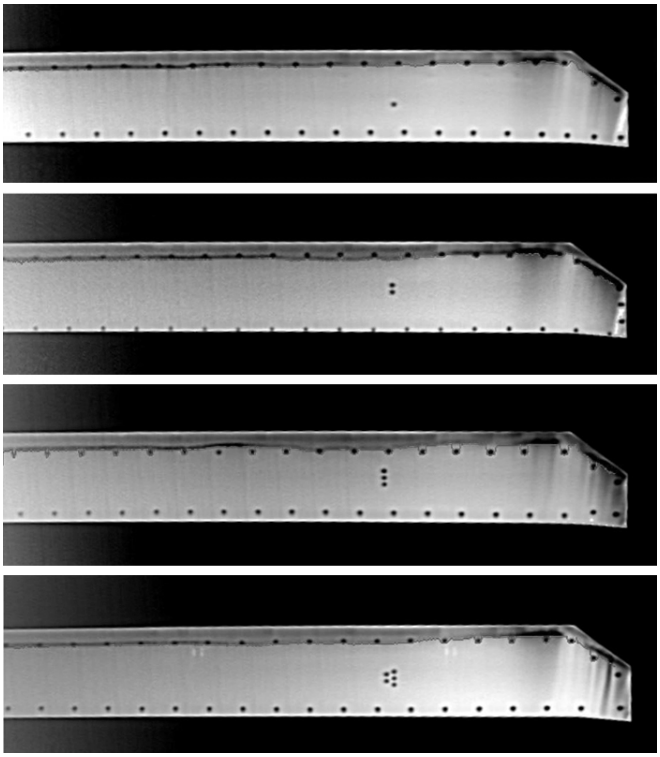

Figure 30. Enhanced thermal images of the upper surface for each blade at M_{tip}=0.65 and θ_0=12°.

As expected for this high thrust condition (Ref. 40), the images indicate the boundary layer flow is primarily turbulent on the upper surface and laminar on the lower surface (as defined by the change in intensities). The upper surface images (Fig. 30) are consistent with one another, indicating transition near x/c=0.20 for all blades. The lower surface images (Fig. 31) show mostly laminar flow except for wedge shaped regions, possibly caused by surface contamination. The locations of the wedges are different for each blade and often change location between runs (the blades were cleaned before every run). The shape of these wedges is interesting in that the wedge angle begins very narrow in the laminar region. As the boundary layer approaches the trailing edge and the region of adverse pressure gradient measured in the pressure distributions, the wedge angle grows wider indicating the transition process is already occurring before the trailing edge. It becomes difficult to visualize transition in this region owing to the low values of skin friction and the likely more gradual amplification of the Tollmien-Schlichting waves.

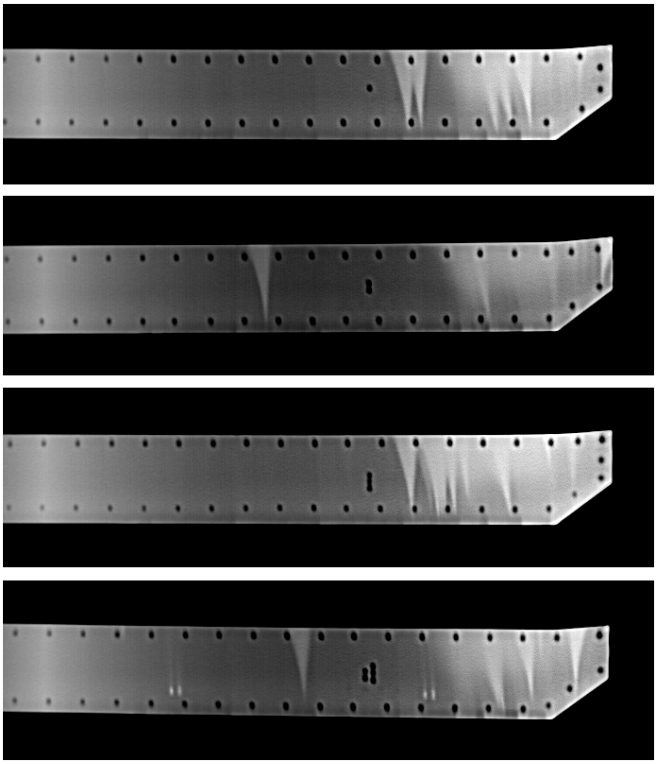

Figure 31. Enhanced thermal images of the lower surface for each blade at M_{tip}=0.65 and θ_0=12°.

Figure 32 shows the estimated upper-surface transition locations (x/c vs. r/R) for each blade, determined through the image processing methods described earlier and depicted in Fig. 12. These traces have been smoothed using a cubic spline with a smoothing factor – the random noise of the image data made for a non-physical, jagged appearance of the transition lines. Also, the ink targets used as fiducials interfered with the intensity profile and the tracing algorithm. These outliers were corrected by hand. No transition figure is provided for the lower surface since it was mostly laminar.

Figures and tabular data for the transition locations (like that shown in Fig. 32) will ultimately be provided for every relevant research condition (Table 3). Early evaluation of the data suggests there are some differences in transition locations between blades, especially at lower collective settings. Examples of these differences at M_{tip}=0.65 and θ_0=6° can be seen in Figs. 33 and 34. It is known that the transition locations for this rotor are highly sensitive to thrust at lower collectives, especially on the lower surface (Ref. 13). Thus, the differences seen in Figs. 33 and 34 are likely due to small differences in blade pitch angles (a result of blade tracking) or small differences in blade aeroelastic properties. Regardless, the transition locations for all blades will be provided in the final database for use in validation.

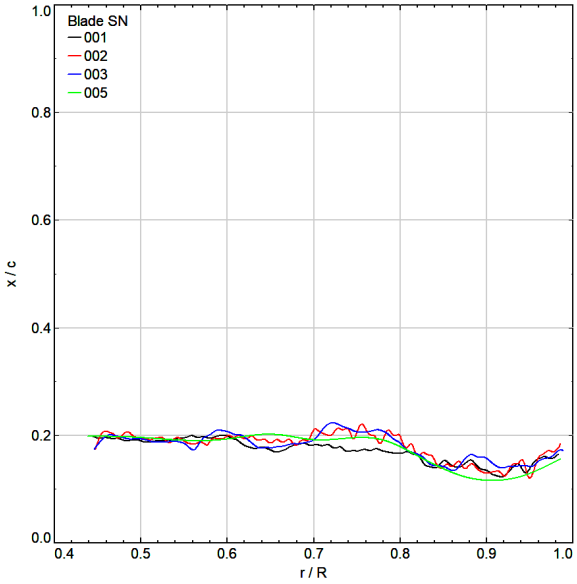

Figure 32. Transition traces of the detected transition of the upper surface for each blade at M_{tip}=0.65 and θ_0=12°. Data are smoothed using a cubic spline with a smoothing factor.

Wake Geometry

Representative tip vortex location measurements are presented in this section for the rotor at M_{tip}=0.65 and θ_0=12° (C_T=0.00993). The shadowgraphy image processing steps described earlier were first applied to the 100 images acquired at each rotor azimuth position (wake age), resulting in identification of the tip vortex centroids in pixel-space coordinates (providing similar results to that shown in Fig. 17). These pixel coordinates were then converted to appropriate blade coordinates and wake age.

Following this approach for the sample test condition results in plots for the radial (Fig. 35a) and axial (Fig. 35b) positions of the tip vortices (in blade coordinates) as a function of wake age. Both the radial and axial positions of the vortices follow the general trends predicted by Landgrebe (Ref. 41). Figure 35a does suggest, however, that the wake on the upstream side of the rotor (i.e., left side of the image) contracts slightly slower than the downstream wake, with the differences between upstream and downstream vortex positions increasing with increasing wake age.

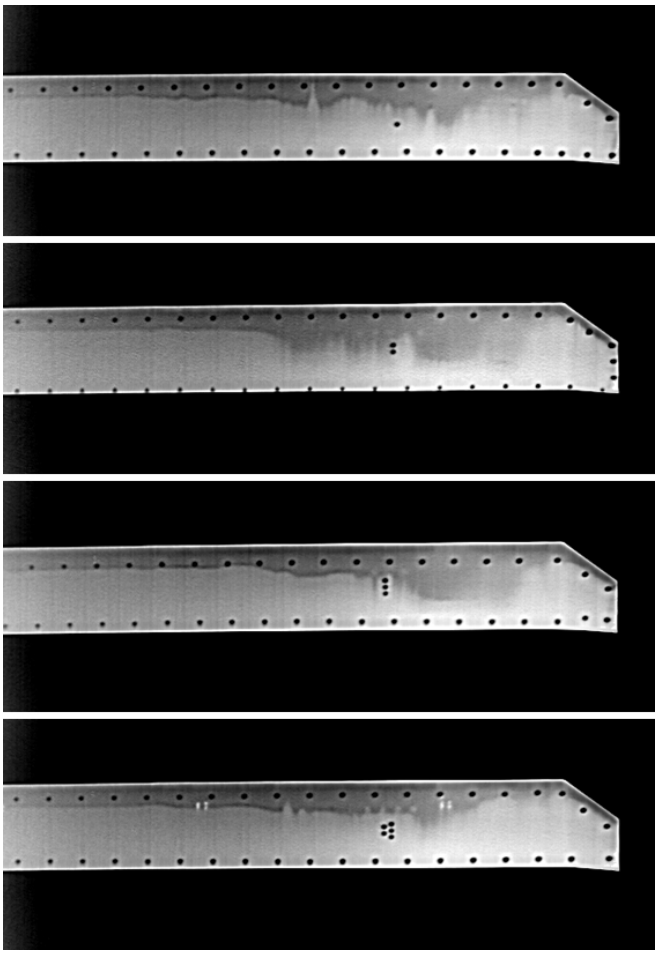

Figure 33. Enhanced thermal images of the upper surface for each blade at M_{tip}=0.65 and θ_0=6°.

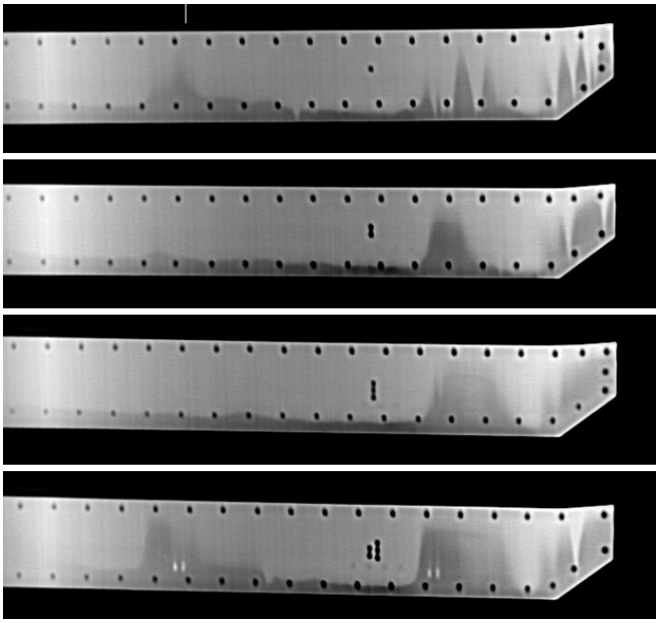

Figure 34. Enhanced thermal images of the lower surface for each blade at M_{tip}=0.65 and θ_0=6°.

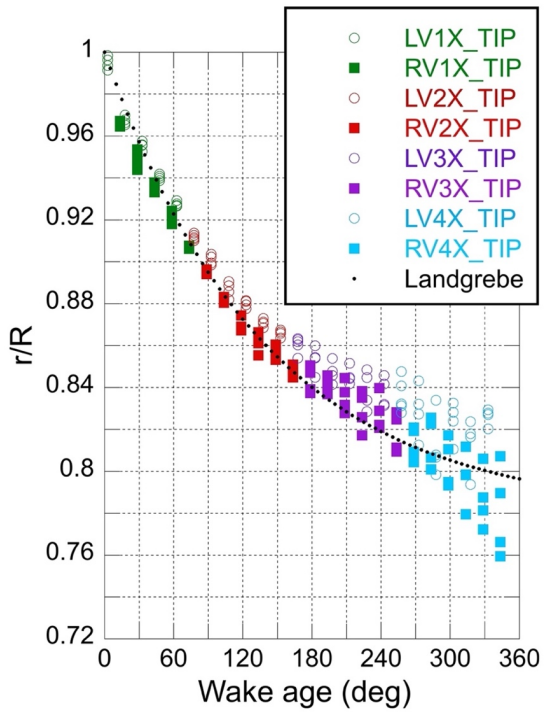

a) Tip vortex: radial position

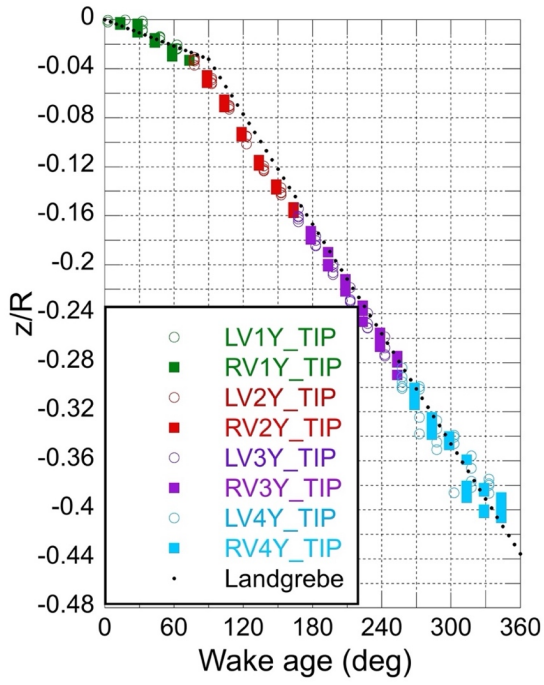

b) Tip vortex: axial position

Figure 35. Wake geometry for M_{tip}=0.65, θ_0=12° (C_T=0.00993). RVn and LVn refer to the vortices appearing on the right (downstream) and left (upstream) sides, respectively, of the shadowgraphy image; n refers to the vortex number.

Efforts are underway to determine the possible sources(s) for these radial contraction differences, which could include errors in the image processing method and/or physical differences in the rotor wake. One such effort was to determine if the GSG vortex-centroiding approach may be introducing a bias in the results. This was evaluated by comparing the GSG results with those derived by manually extracting the vortex positions for all 100 images at a specified condition and rotor azimuth. Both the manual and GSG results indicate a similar amount of asymmetry in the wake and thus the GSG vortex extraction approach is not causing the observed differences. Another possible source for the differences is the calculation of wake age, where the camera offset angle has the largest effect. The radial positions of the upstream and downstream vortices are very sensitive to this offset angle – recall the geometry shown in Fig. 18; however, there is currently no justification to revise this angle (5.38°). It is also possible that there are true physical differences in the rotor wake due to a small, steady crossflow in the tunnel (resulting from the non-symmetric boundary conditions at either end of the wind tunnel test section). There is currently no data confirming this, however.

Efforts to finalize the data reduction approach and further investigate the small radial contraction differences are continuing. A final summary of this effort will be provided along with the data in the final database.

Blade Pressures and Airloads

Figure 36 provides sample chordwise pressure coefficient data for a single radial station (r/R=0.928) at M_{tip}=0.65 and θ_0=12°. Each data point represents the average of data resampled to 256 samples/rev for 166 revs. The variability due to recirculation is evident when comparing the values for each of the ten data points acquired at the same condition (data acquired over a 5-min period). The average of these ten data points at each condition is also shown in the figure and demonstrates the effectiveness of acquiring data over a longer period.

Figure 37 provides the mean chordwise pressure distributions for each of the 11 instrumented radial stations. Error bars are also included, accounting for the separate error sources from the transducer calibration, check points, and the 95% confidence interval for the 10-point averages. As discussed earlier, several transducers were not functioning or found to be invalid during testing and are therefore not included in the plots. The radial station r/R=0.823 is the station with the fewest working transducers.

For analysis validation, comparisons can be made directly with the measured pressure data or eventually with blade airloads computed by integrating the pressures over the blade surface. Integrated airload data will be included, for the stations with sufficient functioning transducers, with the final database.

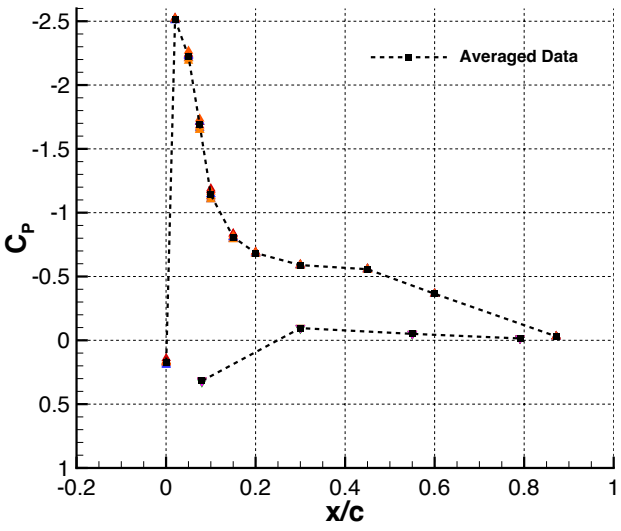

Figure 36. Cp distribution at r/R=0.928 (Station 8) for M_{tip}=0.65 and θ_0=12° (nominal RPM=1250). Includes data from individual data points as well as averages.

DESCRIPTION OF FINAL DATABASE

All the validation-quality data acquired for the configurations and test conditions outlined in Table 3 will be processed and made publicly available on a NASA-sponsored website in the summer of 2023. The final database will include the final averaged data for all measurements for all test conditions in both tabular and graphical forms. The data from individual data points used to generate these averages will also be provided, including data and images for individual blades.

CONCLUDING REMARKS

A model-scale hover test of a 4-bladed, 11.08-ft diameter rotor was recently completed inside the NFAC 80- by 120-Foot Wind Tunnel test section to provide a comprehensive set of measurements for CFD tool validation. Key measurements were acquired for a range of tip Mach numbers and collective settings and included rotor performance, blade airloads, blade transition locations, blade deformations, and wake geometry. The present paper has provided an overview of the test, including detailed descriptions of the hardware, instrumentation, and measurement systems. In addition, the test objectives, approach, and sample results were presented.

Evaluations of the data acquired suggest that the data quantity and quality has met the original objectives for the test and the data set should prove to be a valuable resource to the CFD community for validation. Future work includes final processing of all validation-quality data and posting of all data on a NASA-sponsored website in the summer of 2023.

Author contacts:
Thomas R. Norman, tom.norman@nasa.gov
James T. Heineck, james.t.heineck@nasa.gov
Edward T. Schairer, edward.t.schairer@nasa.gov
Norman W. Schaeffler, n.w.schaeffler@nasa.gov
Lauren N. Wagner, lauren.n.wagner@nasa.gov
Gloria K. Yamauchi, gloria.k.yamauchi@nasa.gov
Austin D. Overmeyer, austin.d.overmeyer.civ@army.mil
Michelle Dominguez, michelle.dominguez@nasa.gov
Alex L. Sheikman, alex.l.sheikman@nasa.gov
Christopher Cameron, christopher.g.cameron.civ@army.mil
Manikandan Ramasamy,
manikandan.ramasamy.civ@army.mil

ACKNOWLEDGMENTS

The authors gratefully acknowledge the significant efforts of the project partners (NASA, U.S. Army) as well as the U.S. Air Force, in the planning, preparation, and execution of this test, particularly Susan Gorton (NASA) and Oliver Wong (U.S. Army) for the decade-long support and advocacy for this entire research effort. Special acknowledgements are made to the NASA/Army team at Langley Research Center (Samantha Zauber, Peter Copp, Joe Miller, Andrew Sawyer, Matt Mueller, W. Derry Mace, and Bryan Mann) for the modification and checkout of the test stand and the design and fabrication of the research blade set. The NASA/Army team at Ames Research Center (Gina Willink, Stephen Wright, Ethan Romander, and Patrick Flynn) are acknowledged for their significant efforts in the preparation for and conduct of the NFAC testing. The U.S. Air Force team (led by Scott Edwards and Paul Gilles, and including Farid Haddad, Jon Winegar, Daniel Brookbank, and Shawn Abadajos) are gratefully acknowledged for making the test run smoothly. The efforts of the additional on-site optics team members (Hannah Spooner, David Keil, and Matt Nguyen) and the DLR Göttingen consultants (Markus Raffel and Christian Wolf, through the NASA-DLR MoU Arrangement for optical systems development for rotorcraft research) deserve special recognition for their key contributions to the success of this program. In addition, the expertise of Advanced Technologies Incorporated in the challenging design, fabrication, and repair of the research blade set is gratefully acknowledged. And finally, special recognition is given to the late Frank Caradonna for his original design of the ARTS and the vision of a benchmark hover test.

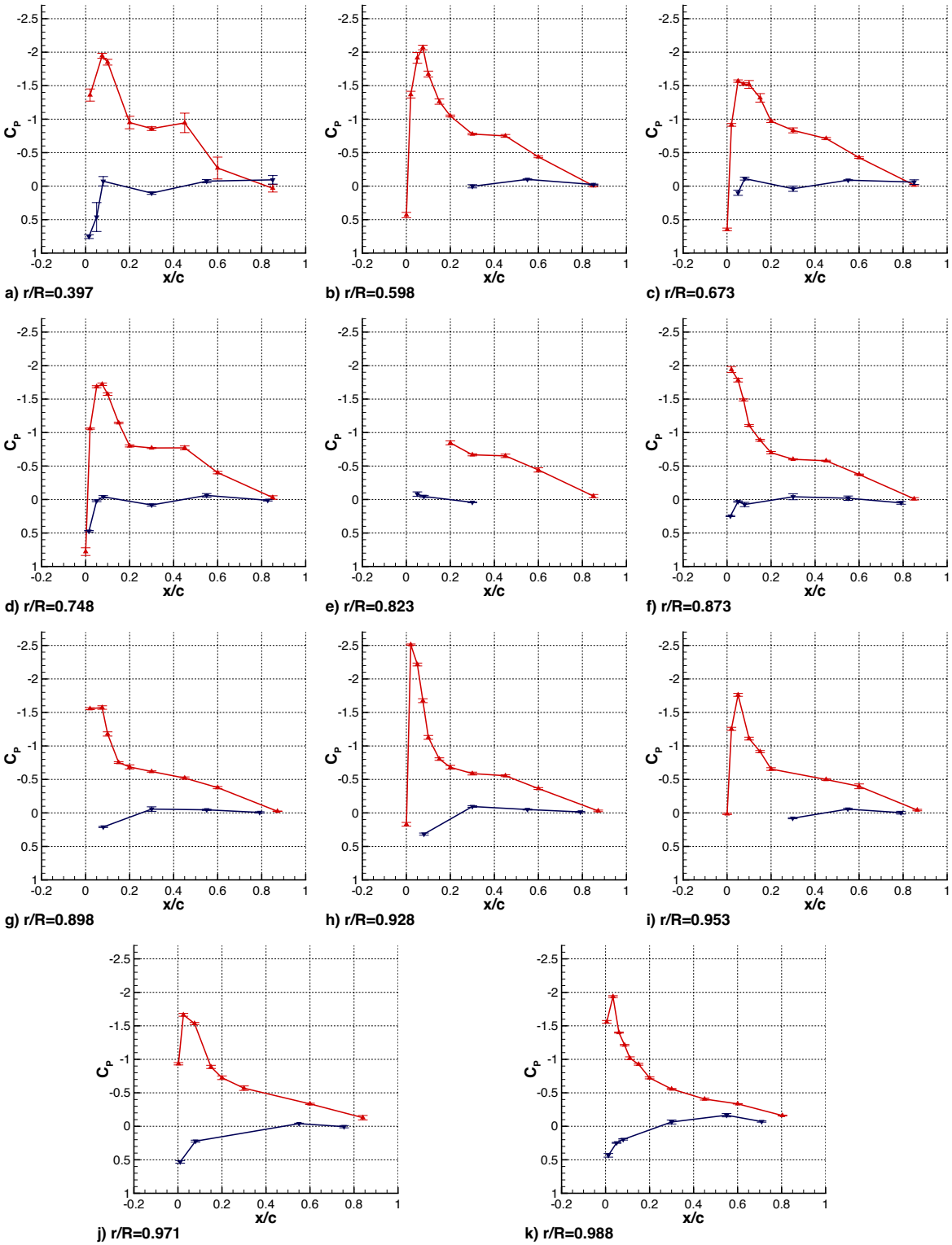

Figure 37. Cp distribution (red upper surface, blue lower surface) at each of the 11 instrumented blade stations for M_{tip}=0.65 and θ_0=12° (nominal RPM=1250). Non-functioning and invalid transducers are not plotted.

REFERENCES

1. Yamauchi, G. K. and Young, L. A., editors, "A Status of NASA Rotorcraft Research," NASA/TP-2009-215369, 2009, pp 22-28, pp 158-160. DOI: 2060/20190002639
2. Hariharan, N., Egolf, T. A., Sankar, L. N., "Simulation of Rotor in Hover: Current State and Challenges," AIAA-2014-0041, AIAA SciTech 52nd Aerospace Sciences Meeting, National Harbor, MD, 13-17 January 2014. DOI: 10.2514/6.2014-0041
3. https://www.aiaa-hpw.org (3-10-2023)
4. Egolf, T. A., Hariharan, N., and Narducci, R., "AIAA Standardized Hover Simulation: Hover Performance Prediction Status and Outstanding Issues," AIAA-2017-1429, AIAA SciTech 55th Aerospace Sciences Meeting, Grapevine, TX, 9-13 January 2017. DOI: 10.2514/6.2017-1429
5. Narducci, R. P., Jain, R., Abras, J., and Hariharan, N., "HVAB Rotor Hover Computational Prediction: A Comparative Study Using OVERFLOW and HPCMP CREATE-AV Helios," Paper AIAA 2021-0617, AIAA 2021 SciTech Forum, Virtual Event, 11-15 and 19-21 January 2021. DOI: 10.2514/6.2021-0617
6. Caradonna, F.X. and Tung, C., "Experimental and Analytical Studies of a Model Helicopter Rotor in Hover," NASA TM 81232, 1981. DOI: 2060/19820004169
7. Johnson, J. L. and Young, L. A., "Tilt Rotor Aeroacoustic Model Project," Confederation of European Aerospace Societies (CEAS), Forum on Aeroacoustics of Rotorcraft and Propellers, Rome, Italy, June 1999.
8. Swanson, S. M., McCluer, M. S., Yamauchi, G. K., and Swanson, A. A., "Airloads Measurements from a 1/4-Scale Tiltrotor Wind Tunnel Test," 25th European Rotorcraft Forum, Rome, Italy, September 1999.
9. Lorber, P. F., Stauter, R. C., and Landgrebe, A. J., "A Comprehensive Hover Test of the Airloads and Airflow of an Extensively Instrumented Model Helicopter Rotor," American Helicopter Society 45th Annual Forum Proceedings, Boston, MA, May 1989.
10. Lorber, P. F., "Aerodynamic Results of a Pressure-Instrumented Model Rotor Test at the DNW," American Helicopter Society 46th Annual Forum Proceedings, Washington D.C., May 1990.
11. Balch, D. T., "Experimental Study of Main Rotor Tip Geometry and Tail Rotor Interactions in Hover. Volume 1. Test and Figures," NASA CR 177336, 1985. DOI: 2060/19850014034
12. Balch, D. T., "Experimental Study of Main Rotor Tip Geometry and Tail Rotor Interactions in Hover. Volume 2. Run Log and Tabulated Data," NASA CR 177336, 1985. DOI: 2060/19850014035
13. Overmeyer, A. D. and Martin, P. B., "Measured Boundary Layer Transition and Rotor Hover Performance at Model Scale," AIAA-2017-1872, AIAA SciTech 55th Aerospace Sciences Meeting, Grapevine, TX, 9-13 January 2017. DOI: 10.2514/6.2017-1872
14. Chaderjian, N. M., and Ahmad, J. U., "Navier-Stokes Assessment of Test Facility Effects on Hover Performance," American Helicopter Society 71st Annual Forum Proceedings, Virginia Beach, VA, May 2015.
15. Jain, R., "Effect of Facility Walls and Blade Aeroelasticity on PSP Rotor Hover Performance Predictions," AIAA-2018-0305, AIAA SciTech 56th Aerospace Sciences Meeting, Kissimmee, FL, 8-12 January 2018. DOI: 10.2514/6.2018-0305
16. Fulton, M. V., Gold, N. P., Nielsen, G. E., Mansur, M. M., Tischler, M. B., and Domzalski, D. B., "Development and Hover Testing of the Active Elevon Rotor," American Helicopter Society 68th Annual Forum Proceedings, Fort Worth, TX, May 2012.
17. Wong, O. D., Noonan, K. W., Watkins, A. N., Jenkins, L. N., and Yao, C. S., "Non-Intrusive Measurements of a Four-Bladed Rotor in Hover - A First Look," American Helicopter Society Aeromechanics Specialists Conference, San Francisco, CA, January 2010.
18. Overmeyer, A. D., Copp, P. A., and Schaeffler, N. W., "Hover Validation and Acoustic Baseline Blade Set Definition," NASA TM-2020-5002153, May 2020. DOI: 2060/20205002153
19. Schairer, E.T., Heineck, J.T., Spooner, H., and Overmeyer, A.D., "Blade Displacement Measurements of a Rotor in Forward Flight in the Langley 14- by 22-Foot Wind Tunnel," AIAA Paper 2021-0131, AIAA 2021 SciTech Forum, Virtual Event, 11-15 and 19-21 January 2021. DOI: 10.2514/6.2021-0131
20. Abrego, A.I., Meyn, L., Burner, A.W., and Barrows, D.A., "Summary of Full-Scale Blade Displacements of the UH-60A Airloads Rotor," American Helicopter Society Technical Meeting on Aeromechanics Design for Vertical Lift, San Francisco, CA, January 2016. DOI: 2060/20160007400
21. Fleming, G. A., "RASP: Rotor Azimuth Synchronization Program (RASP) User's Guide, Version 1.3," NASA Langley Research Center, February 6, 2008.
22. https://www.geodetic.com/v-stars/ (3-10-2023)
23. Wolf, P.R., *Elements of Photogrammetry*, McGraw-Hill, New York, NY, 1974.
24. Mikhail, E.M., Bethel, J.S., and McGlone, J.C., *Introduction to Modern Photogrammetry*, John Wiley & Sons, Inc., New York, NY, 2001.
25. Zhang, Z., "Flexible Camera Calibration by Viewing a Plane from Unknown Orientations," International Conference on Computer Vision, Corfu, Greece, September 1999, pp. 666–673. DOI: 10.1109/ICCV.1999.791289
26. Liu, T. and Burner, A.W., "Photogrammetry Toolbox Reference Manual," NASA CR-2014-218518, September 2014. DOI: 2060/20140012781
27. Hartley, R. and Zisserman, A., *Multiple View Geometry in Computer Vision*, Cambridge University Press, 2000.
28. Quast, A. "Detection of transition by infrared image technique," 12th International Congress on Instrumentation in Aerospace Simulation Facilities Proceedings, Williamsburg, VA, 22-25 June 1987, pp 125-134.
29. Carlomagno, G. M. and Cardone, G., "Infrared thermography for convective heat transfer

measurements," *Experiments in Fluids*, Vol. 49, No. 6, 2010, pp. 1187-1218. DOI: 10.1007/s00348-010-0912-2
30. Overmeyer, A., Heineck, J.T., and Wolf, C.C., "Unsteady Boundary Layer Transition Measurements of a Rotor in Forward Flight," American Helicopter Society International 74th Annual Forum Proceedings, Phoenix, AZ, May 2018.
31. Heineck, J. T., Spooner, H., Overmeyer, A., Gardner, A., Weiss, A., and Raffel, M., "Transition Measurements of Upper and Lower Rotor Blade Surfaces in Forward Flight with Thermography," AIAA-2020-3103, AIAA 2020 Aviation Forum, Virtual Event, 15-19 June 2020. DOI: 10.2514/6.2020-3103
32. Richter, K. and Schlein, S., "Boundary-Layer Transition Measurements on Hovering Helicopter Rotors by Infrared Thermography", *Experiments in Fluids*, Vol. 55, No. 7, July 2014. DOI: 10.1007/s00348-014-1755-z
33. Gardner, A, Wolf, C.C., Heineck, J.T., Barnett, M., and Raffel, M., "Helicopter Rotor Boundary Layer Transition Measurement in Forward Flight Using an Infrared Camera," VFS 75th Annual Forum Proceedings, Philadelphia, PA, May 2019.
34. Wolf, C.C., Gardner, A., and Raffel, M., "Infrared Thermography for Boundary Layer Transition Measurements," *Measurement Science and Technology*, 31 112002, 2020. DOI: 10.1088/1361-6501/aba070
35. Raffel M., and Heineck, J.T., "Mirror-Based Image Derotation for Aerodynamic Rotor Measurements," *AIAA Journal*, Vol. 52, No. 6, 2014. DOI: 10.2514/1.J052836
36. Richter, K, Wolf, C.C., Gardener, A.D., and Merz, C.B. "Detection of Unsteady Boundary Layer Transition Using Three Experimental Methods", AIAA-2016-1072, AIAA SciTech 54th Annual Aerospace Sciences Meeting, San Diego, CA, 4-8 January 2016. DOI: 10.2514/6.2016-1072
37. Norman, T. R. and Light, J. S., "Rotor Tip Vortex Geometry Measurements Using the Wide-Field Shadowgraph Technique," *Journal of the American Helicopter Society*, Volume 32, Number 2, April 1987, pp. 40-50(11). DOI: 10.4050/JAHS.32.40
38. Light, J. S., "Tip Vortex Geometry of a Hovering Helicopter Rotor in Ground Effect," *Journal of the American Helicopter Society*, Volume 38, Number 2, April 1993, pp. 34-42(9). DOI: 10.4050/JAHS.38.34
39. Light, J. S., Swanson, A. S., and Norman, T. R., "Application of the Wide-Field Shadowgraph Technique to Helicopters in Forward Flight," *Journal of the American Helicopter Society*, Volume 37, Number 2, April 1992, pp. 23-28(6). DOI: 10.4050/JAHS.37.23
40. Overmeyer, A. and Martin, P., "The Effect of Laminar Flow on Rotor Hover Performance," American Helicopter Society International 74th Annual Forum Proceedings, Phoenix, AZ, May 2018.
41. Landgrebe, A. J., "The Wake Geometry of a Hovering Helicopter Rotor and Its Influence on Rotor Performance," *Journal of the American Helicopter Society*, Volume 17, Number 4, October 1972, pp. 3-15(12). DOI: 10.4050/JAHS.17.4.3